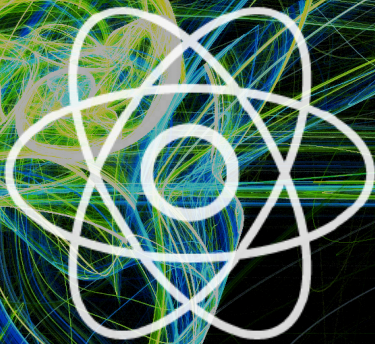


**JOURNAL OF ENGINEERING
RESEARCH & SCIENCES**

JENRS



**www.jenrs.com
ISSN: 2831-4085**

**Volume 5 Issue 4
April 2026**

EDITORIAL BOARD

Editor-in-Chief

Dr. Jinhua Xiao

Department of Industrial Management
Politecnico di Milano, Italy

Editorial Board Members

Dr. Jianhang Shi

Department of Chemical and Biomolecular
Engineering, The Ohio State University, USA

Dr. Sonal Agrawal

Rush Alzheimer's Disease Center, Rush
University Medical Center, USA

Prof. Kamran Iqbal

Department of Systems Engineering, University
of Arkansas Little Rock, USA

Dr. Anna Formica

National Research Council, Istituto di Analisi dei
Sistemi ed Informatica, Italy

Prof. Anle Mu

School of Mechanical and Precision Instrument
Engineering, Xi'an University of Technology,
China

Dr. Qichun Zhang

Department of Computer Science, University of
Bradford, UK

Dr. Żywiołek Justyna

Faculty of Management, Czestochowa University
of Technology, Poland

Dr. Diego Cristallini

Department of Signal Processing & Imaging
Radar, Fraunhofer FHR, Germany

Ms. Madhuri Inupakutika

Department of Biological Science, University of
North Texas, USA

Dr. Jianhui Li

Molecular Biophysics and Biochemistry,
Yale University, USA

Dr. Lixin Wang

Department of Computer Science,
Columbus State University, USA

Dr. Unnati Sunilkumar Shah

Department of Computer Science, Utica
University, USA

Dr. Ramcharan Singh Angom

Biochemistry and Molecular Biology,
Mayo Clinic, USA

Dr. Prabhash Dadhich

Biomedical Research, CellfBio, USA

Dr. Qiong Chen

Navigation College, Jimei University, China

Dr. Mingsen Pan

University of Texas at Arlington, USA

Dr. Haiping Xu

Computer and Information Science
Department, University of Massachusetts
Dartmouth, USA

Prof. Hamid Mattiello

Department of Business and Economics,
University of Applied Sciences (FHM),
Germany

Dr. Deepak Bhaskar Acharya
Department of Computer Science, The University
of Alabama in Huntsville, USA

Dr. Gabriel-Alexandru Constantin
Department of Biotechnical Systems, Faculty of
Biotechnical Systems Engineering, National
University of Science and Technology
POLITEHNICA Bucharest, Romania

Prof. Rashid A Saeed
Scientific Research Deanship, Lusail University,
Qatar

Prof. Cheng-Chi Lee
Department of Library and Information Science,
Fu Jen Catholic University, Taiwan

Prof. Marian Pompiliu Cristescu
Finance Accounting Department, Lucian Blaga
University of Sibiu, Romania

Dr. Shabir Ahmad
Department of Mathematics and Physics,
University of Campania Luigi Vanvitelli, Italy

Dr. Serdar Halis
Department of Automotive Engineering,
Pamukkale University, Turkey

Dr. Sarat Chandra Mohapatra
Centre for Marine Technology and Ocean
Engineering (CENTEC), Instituto Superior
Técnico/University of Lisbon, Portugal

Dr. Amin Amiri Delouei
Department of Mechanical Engineering,
University of Bojnord, Iran

Dr. Alexander Chupin
Faculty of Economics, RUDN University, Russia

Prof. Wafaa Mohammed Ridha
Technical Institute of Babylon, Al-Furat Al-Awsat
Technical University, Iraq

Dr. Ali Golestani Shishvan
Department of Electrical & Computer
Engineering, University of Toronto,
Canada

Prof. Abdeltif Amrane
Institute of Chemical Sciences of Rennes,
University of Rennes, France

Prof. Ahmad M. A. zamil
Department of Marketing, Prince Sattam
bin Abdulaziz University, Saudi Arabia

Dr. Lilik Jamilatul Awal
Faculty of Advanced Technology and
Multidiscipline, Airlangga University,
Indonesia

Dr. Behrokh Beiranvand
TEKsystems at Apple Inc, Contractor at
Apple Inc, United States

Prof. Giuseppe Oliveto
Department of Engineering, University of
Basilicata, Italy

Dr. Saad khadar
Electrical Engineering Department,
University of Djelfa, Algeria

Dr. Ali Moghassemi
Electrical Engineering, University of
Wisconsin-Milwaukee, United States

Dr. Fan Xu
Shenzhen Institute for Advanced Study,
University of Electronic Science and
Technology of China, China

Prof. Juan Eduardo Nápoles Valdes
Matemáticas, Universidad Nacional del
Nordeste, Argentina

Dr. Parveen Berwal
Civil Engineering, Galgotias College of
Engineering and Technology, Greater
Noida, India

Prof. Filipe Almeida Correa do Nascimento
Transportation Engineering Program, Instituto Militar de Engenharia (Military Institute of Engineering), Brazil

Mr. Anderson Apolônio Lira Queiroz
Center Computer, Universit Federal Pernambuco, Brazil

Dr. Sachin Kumar
Electronics and Communication Engineering, Galgotias College of Engineering and Technology, India

Dr. Ram Prasad
Department of Botany, Mahatma Gandhi Central University, India

Dr. Juan Molina
Departamento de Biología Bioquímica y Farmacia, Universidad Nacional del Sur, Argentina

Prof. Alexander E. Hramov
Research Institute of Applied AI and Digital Solutions, Plekhanov Russian University of Economics, Russia

Dr. Alina Alb Lupas
Department of Mathematics and Computer Science, University of Oradea, Romania

Prof. Waluyo
Department of Electrical Engineering, Institut Teknologi Nasional Bandung, Indonesia

Prof. Marco Milanese
Department of Engineering for Innovation, University of Salento, Italy

Dr. Seyit Uguz
Department of Biosystems Engineering, Yozgat Bozok University, Turkey

Dr. Alejandro Medina Santiago
Computer Science, Institute National of Astrophysic, Optics and Electronics, Mexico

Prof. Chi-Wai Chow
Department of Photonics, National Yang Ming Chiao Tung University, Taiwan

Dr. Marius Stef
Department of Physics, West University of Timisoara, Romania

Dr. George Dănut Mocanu
Team Sports Games and Physical Education, Dunărea de Jos University, Romania

Dr. André Saandim
Departamento de Ciências Florestais, Universidade de Trás-os-Montes e Alto Douro, Portugal

Prof. Juan Antonio López Ramos
Department of Mathematics, University of Almeria, Spain

Dr. hanan Mikhael Dawood Habbi
Department of Electrical Engineering, University of Baghdad, Iraq

Prof. Aissani Amar
Dept Artificial Intelligence & Data Science, University of Science & Technology Houari Boumediene (USTHB), Algeria

Prof. Rabha W. Ibrahim
Develop Researchs Departement, SAS, United States

Dr. Fathurrahman Lananan
Faculty of Bioresources and Food Industries, Universiti Sultan Zainal Abidin (UniSZA), Malaysia

Dr. Bhupendra Kumar Singh
Division of Advanced Nuclear Engineering, Pohang University of Science and Technology (POSTECH), South Korea

Dr. Fazlur Rahman
Faculty of Built Environment and Surveying, Universiti Teknologi Malaysia, Malaysia

Prof. Rupesh Kumar

Jindal Global Business School, O P Jindal Global University, India

Prof. Laura Eugenia Paulette

Faculty of Agriculture, Technical and soil sciences, University of Agricultural Sciences and Veterinary Medicine Cluj Napoca, Romania

Dr. Ana Maria Mihaela Iordache

Informatics, Statistics and Mathematics, Romanian American University, Romania

Dr. V.I. Zhukov

Department of Chemistry and Chemical Technology, Novosibirsk State Technical University, Russia

Dr. Ammar Mohammad Jamil Odeh

King Hussein School of Computing Sciences, Princess Sumaya University for Technology, Jordan

Prof. Pshtiwan Othman Mohammed

College of Education, University of Sulaimani, Iraq

Dr. Alex Rizzato

Department of Biomedical Sciences, University of Padova, Italy

Dr. Farrukh Shahzad

School of Economics and Management, Guangdong University of Petrochemical Technology, China

Dr. Esra Calik Bayazit

Computer Engineering, Fatih Sultan Mehmet Vakif University

Prof. Osamah Ibrahim Khalaf

Al-Nahrain Renewable Energy Research Center, Al-Nahrain University

Prof. Acácio Manuel Raposo Amaral

Coimbra Institute of Engineering, Polytechnic Institute of Coimbra

Dr. Laura Gioiella

School of Architecture and Design, University of Camerino, Italy

Dr. Hamzeh Mehrabi

College of Science, University of Tehran, Iran

Dr. Hakim Mellah

Computer Science and Software Engineering Department, Concordia University, Canada

Dr. Maha AbouBakr Ibrahim

Faculty of Engineering, Architectural engineering department, Misr University for Science and Technology, Egypt

Prof. Maged S. Al-Fakeh

Department of Chemistry, Qassim University, Saudi Arabia

Prof. Boris F. Minaev

Arrenius Laboratory, Uppsala University, Sweden

Dr. Ermelinda Kordha

Department of Marketing and Tourism, University of Tirana, Albania

Prof. Francesco Inchingolo

Interdisciplinary of Medicine, University of Bari Aldo Moro, Italy

Prof. Alban Kuriqi

Civil Engineering, University for Business and Technology

Dr. Papa Pio Ascona Garcia

Profesional De Ingenieria Civil, Universidad Nacional Intercultural, Fabiola Salazar Leguía

Prof. Wael A. Altabey

Department of Mechanical Engineering, Alexandria University

Dr. A B M Amrul Kaish

Department of Civil Engineering, Universiti
Kebangsaan Malaysia

Prof. Vitalii Ivanov

Manufacturing Engineering, Machines and Tools,
Sumy State University

Ms. Beknazarova Saida Safibullayevna

Television and media technologies, Tashkent
university of information technologies

Prof. Chow Ming Fai

Department of Civil Engineering, Monash
University Malaysia

Dr. Mojtaba Fardi

Department of Applied Mathematics, Shahrekord
University

Dr. Takele Ferede Agajie

School of Electrical and Computer Engineering,
Institute of Technology, Debre Markos University

Prof. Ebenezer Esenogho

Centre for Artificial Intelligence and
Multidisciplinary Innovations, University of
South Africa

Dr. Lim Chen Kim

Institute of Environment and Development
(LESTARI), Universiti Kebangsaan Malaysia
(UKM)

Mr. Sushant K. Rawal

Department of Mechanical Engineering,
McMaster University

Dr. Crescenzo Pepe

Dipartimento di Ingegneria dell'Informazione,
Università Politecnica delle Marche

Prof. Bucur Daniel

Department: Pedotechnics, Iasi University of Life
Sciences

Dr. Adeb Ali Mohammed Ahmed Al-Samet

Faculty of Information and
Communication Technology, Universiti
Tunku Abdul Rahman

Dr. Abhishek Phadke

School of Engineering and Computing,
Christopher Newport University

Dr. Zishan Shaikh

Department of Environmental Science,
Savitribai Phule Pune University

Dr. Sofiane HADDAD

Electronic Department, MSB Jijel
University

Dr. Tibor Krenicky

Faculty of Manufacturing Technologies
with a seat in Prešov, Technical University
of Košice

Prof. Denys Baranovskyi

Department of Computerization and
Robotization of Industrial Processes,
Rzeszow University of Technology

Prof. Mejdi Snoussi

College of Science, Biology Department,
University of Hail

Prof. YoungPak Lee

Physics/Optical Science and Engineering,
Hanyang University

Prof. Mohamed Mohamed Zaky Ahmed

College of Engineering/Department of
Mechanical Engineering, Prince Sattam
bin Abulaziz University

Dr. Maryna Bulakh

Department of Computerization and
Robotization of Industrial Processes,
Rzeszow University of Technology

Prof. Ion Sandu

Arheoinvest Research Platform, Alexandru
Ioan Cuza University of Iasi

Dr. Muhammad Imran Khan
Institute of Soil and Environmental Sciences,
University of Agriculture Faisalabad

Prof. Hui Liu
School of Artificial Intelligence, Nanjing
University of Information Science and
Technology

Mr. Noor Mohammad Mohammad
School of Mechanical Engineering, Purdue
University

Dr. Naeem Saleem
Department of Mathematics, University of
Management and Technology

Dr. Israr Ahmad
Coppin State University

Editorial

The *Journal of Engineering Research and Sciences (JERS)* is pleased to present a collection of research contributions that demonstrate the breadth of contemporary engineering research and its growing impact on both advanced technological systems and everyday applications. The studies featured in this issue address critical challenges in explainable artificial intelligence, predictive maintenance, fluid mechanics, and product design. Through the integration of data-driven methodologies, analytical modeling, and practical engineering solutions, these contributions advance scientific understanding while offering tangible benefits for industry and society.

As artificial intelligence becomes increasingly embedded within modern data center operations, the need for transparency and trust in machine learning models has emerged as a critical concern. One contribution investigates the application of explainable artificial intelligence techniques within a large-scale solid-state drive failure prediction framework. Utilizing extensive real-world data from more than half a million SSDs, the study evaluates the effectiveness of LIME and SHAP in enhancing model interpretability while maintaining predictive performance. By integrating explainability into a cost-sensitive maintenance strategy, the research demonstrates substantial operational savings and improved decision support for data center management. The findings highlight the importance of transforming traditionally opaque machine learning systems into transparent and verifiable tools capable of supporting reliable industrial operations. [1]

Fluid mechanics continues to provide valuable insights into the design and optimization of everyday consumer products. A detailed investigation into the discharge behavior of viscous liquid detergents examines the influence of outlet geometry, material characteristics, viscosity, and air-vent configurations on flow performance. Combining theoretical analysis based on hydrostatic pressure and Bernoulli's principle with extensive numerical simulations and experimental observations, the study identifies outlet radius as the dominant factor governing discharge volume while emphasizing the stabilizing role of air vents. The findings contribute to a deeper understanding of viscous-fluid transport and offer practical guidance for the design of household dispensing systems, automatic detergent delivery devices, and other applications requiring precise fluid control. [2]

The contributions presented in this issue underscore the value of combining theoretical rigor with practical innovation to address challenges across diverse engineering domains. From improving the transparency and trustworthiness of artificial intelligence systems in critical infrastructure to enhancing the performance of consumer products through fluid mechanics principles, these studies exemplify the role of engineering research in advancing technology and improving quality of life. It is hoped that the findings reported herein will stimulate further inquiry, encourage interdisciplinary collaboration, and contribute to the continued advancement of engineering science and practice.

References:

- [1] S.K. Kumar, "Explainable AI for SSD Failure Prediction: Using LIME and SHAP for Transparency," *Journal of Engineering Research and Sciences*, vol. 5, no. 4, pp. 1-16, 2026, doi:10.55708/js0504001.
- [2] Y. Kwon, E. Jekal, "An Extended Investigation of Detergent Bottle Structure Based on Fluid Mechanics," *Journal of Engineering Research and Sciences*, vol. 5, no. 4, pp. 17-23, 2026, doi:10.55708/js0504002.

Editor-in-chief

Dr. Jinhua Xiao

CONTENTS

<i>Explainable AI for SSD Failure Prediction: Using LIME and SHAP for Transparency</i> Saurav Kant Kumar	01
<i>An Extended Investigation of Detergent Bottle Structure Based on Fluid Mechanics</i> Yeonwoo Kwon and Eunsung Jekal	17

Explainable AI for SSD Failure Prediction: Using LIME and SHAP for Transparency

Saurav Kant Kumar* 

Department of Information Technology, University of the Cumberlands, Williamsburg, KY, 40769, USA

Email(s): sauravkantkumar@gmail.com (S. Kumar)

*Corresponding author: Saurav Kant Kumar, Email: skumar48576@ucumberlands.edu

ABSTRACT: Artificial Intelligence (AI) has become increasingly crucial for modern data centers for automating tasks ranging from anomaly detection to predictive maintenance. Nevertheless, a significant limitation of underlying machine learning (ML) models is their “black box” nature. This lack of transparency limits trust among stakeholders who require visibility into model decisions. We address this lack of transparency by evaluating explainable AI techniques within an SSD failure prediction pipeline to improve interpretability and operational trust. Our study makes the following three main contributions. First, we provide a large-scale empirical evaluation of explainable AI techniques (LIME and SHAP) within an SSD failure prediction pipeline under realistic temporal validation and deployment constraints. Second, we provide a qualitative comparison of LIME and SHAP, focusing on their roles in local and global interpretability and their practical behavior in SSD failure prediction. Third, we analyze model performance from an operational perspective using a cost-sensitive framework, demonstrating how explainability supports decision-making in data center environments. To address temporal data leakage and model robustness, we evaluate our approach on a temporal split with 10,637,778 training records and 5,499,337 test records from the Alibaba dataset, which contains data from over 500,000 SSDs. The tuned XGBoost model achieved a recall of 67.98%, precision of 4.43%, and false alarm rate of 0.1878, by optimizing a custom “Safety-First” cost function at a decision threshold of 0.680, effectively functioning as a high-sensitivity screening tool. This approach resulted in an estimated net operational savings of \$13.42 million compared to baseline maintenance strategies. Additionally, the findings show that LIME generates intuitive, human-readable justifications for individual predictions and SHAP explains the model at both global and local levels. Integration of an explainable AI layer to ML pipelines turns “black box” models into systems that are easy to understand and verify, which makes them more trustworthy and reliable.

KEYWORDS: Predictive Maintenance, SSD Failure Prediction, Model Interpretability, Explainable AI, LIME, SHAP

1. Introduction

Global data volume has grown rapidly in recent years because far more individuals have access to the internet, more people are using cloud computing, and the use of digital devices has exploded. With IDC projecting global data volumes to reach 175 zettabytes (ZB) by 2025, data centers are deploying massive SSD fleets that continuously generate telemetry data, including SMART metrics, wear indicators, latency measurements, and temperature readings [1, 2]. At the same time, the amount of computing power needed for modern AI models has doubled every few months in the past [3]. Because of this, data center technicians must work hard to keep their systems running 100% of the time to make sure they are reliable and don't cause service outages. This necessitates predictive maintenance, anomaly detection, accurate SSD failure prediction, and the use of explainable AI to validate the results [4].

To predict an SSD failure, it's necessary to train complex machine learning (ML) models on telemetry data. However, these models are “black boxes”, which means

it's hard to know how they make predictions [2, 5, 6]. Although these models can be highly accurate, their internal decision-making process is often opaque to users, operations managers, reliability engineers, and compliance teams who must trust and validate the decisions generated by these models [7, 8]. When a model predicts that a specific SSD has a high probability of failure, stakeholders must be able to understand the reasoning behind that prediction. This lack of transparency makes it difficult to verify predictions, ensure accountability, and build confidence in the system [9, 10]. Consequently, there is a need for explainable AI techniques to make SSD failure prediction more interpretable, transparent, and operationally trustworthy [11, 12].

The importance of explainable AI is not limited to operational trust in the model predictions; it is becoming a statutory requirement [7, 9, 13]. Many countries have introduced strong data protection and AI governance frameworks, including the GDPR and AI Act of the EU, CCPA and NIST AI Risk Management Framework in the United States, and global regulations such as PIPEDA (Canada), LGPD (Brazil),

POPIA (South Africa), and China's PIPL [9, 10, 14, 15]. These laws call for transparency, traceability, and accountability in automated systems, thus augmenting the significance of explainable AI methodologies [7, 16]. In the United States, agencies such as the National Institute of Standards and Technology (NIST), the Federal Trade Commission (FTC), and the Cybersecurity and Infrastructure Security Agency (CISA) are developing guidelines for the trustworthy deployment of AI in critical infrastructure, where model interpretability is essential for ensuring safety, auditability, and regulatory compliance [15, 17]. Insufficient or confusing explanations for how a machine-learning model reaches a failure prediction can result in compliance violations, loss of customer and stakeholder trust, and difficulties meeting industry requirements for safety, reliability, and fairness in automated decision-making [9, 10].

Advanced machine learning models used for SSD failure prediction, including ensemble approaches such as Random Forest, XGBoost, and LightGBM, demonstrate strong predictive performance; however, they often lack interpretability [2, 11, 18]. Stakeholders prefer not only accurate predictions of failures that are about to happen, but also detailed explanations of how these predictions are made [8, 12]. From an operational standpoint, stakeholders need to pinpoint exactly which SMART attributes are triggering a failure alert, while also understanding how the model adapts to different SSD vendors and changing workloads [4, 18].

Although LIME and SHAP are widely used post-hoc explanation techniques, there remains limited empirical evidence regarding their effectiveness in large-scale SSD failure prediction systems evaluated under realistic temporal validation constraints. Also, these models must be validated against temporal data leakage to ensure that historical patterns effectively generalize to future failure events.

This paper focuses on the interpretability and operational viability of machine learning models for SSD failure prediction and makes the following contributions:

1. We train and evaluate the performance of Random Forest, XGBoost, and LightGBM using a strict temporal walk-forward split of 16,137,115 telemetry records (10,637,778 training and 5,499,337 test records) spanning 90,761 unique SSDs from the Alibaba dataset. This scale and validation strategy ensure real-world predictive integrity by eliminating the temporal data leakage often introduced by random train-test splits in failure prediction studies.
2. We systematically evaluate LIME and SHAP as diagnostic tools for SSD failure prediction, testing their ability to provide interpretable explanations that support auditing, transparency, and regulatory requirements such as the "Right to Explanation" under frameworks including GDPR and the NIST AI Risk Management Framework.
3. We apply a cost-sensitive decision framework that integrates threshold optimization with an operational cost model, enabling economically efficient failure prediction under asymmetric risk conditions.

4. We evaluate the integration of explainable AI techniques within an SSD failure prediction pipeline to improve interpretability and support operational decision-making.

This paper is structured as follows: Section 2 reviews related work on regulatory frameworks, explainable AI, and SSD failure prediction. Section 3 describes the methodology and proposed system architecture. In Section 4, we show the experimental results, highlighting how effectively the model worked, an assessment of operational costs, and thorough explainability assessments. Section 5 discusses the strategic implications for data center operators, the economic trade-offs of the "Safety-First" approach, and current limitations. Finally, Section 6 concludes the paper.

2. Related Work

Our research takes inspiration from three domains: regulatory frameworks mandating transparency and explainability, advancements in explainable AI methodologies, and the application of machine learning techniques to predict SSD failures.

2.1. Regulatory Frameworks

The rapid advancement and widespread use of AI, together with the focus on transparency and accountability, have led to the development of regulations and standards on how to use AI [7, 9, 10]. The General Data Protection Regulation (GDPR) and the forthcoming AI Act of the European Union mandate a right to explanation and classify high-risk AI systems, such as those used in critical infrastructure, under strict transparency, documentation, and human-oversight requirements [13, 14]. Similarly, U.S.-based agencies such as NIST, the FTC, and CISA have introduced the AI Risk Management Framework and related guidance to promote trustworthy, auditable AI deployment in enterprise environments [15, 17]. These regulatory initiatives highlight the growing need for explainable AI techniques that enable stakeholders to interpret model predictions, support auditing processes, and ensure responsible deployment of machine learning systems in operational environments. These frameworks illustrate how the focus is shifting from how efficiently the models work to how easy they are to understand, evaluate, and be fair in automated decision-making [7].

2.2. Explainable AI Techniques

While ML and DL models for SSD failure prediction have matured and are able to achieve state-of-the-art performance [2, 18], the field of explainable AI (XAI) has increasingly focused on making these models more interpretable and understandable to stakeholders [11, 12]. XAI methods are generally categorized into intrinsically interpretable models, like linear models and decision trees, and post-hoc explanation techniques that aim to interpret complex black-box models after training. There are several post-hoc XAI methods but LIME (Local Interpretable Model-Agnostic Explanations) and SHAP (SHapley Additive exPlanations) are the most widely adopted methods for understanding model behaviour [5, 6].

LIME explains individual predictions by locally approximating the complex model with an interpretable surrogate model, often a simple linear model or decision tree, around the instance of interest [5]. In SSD failure prediction, LIME highlights which SMART attributes most influenced a specific drive's failure score, providing transparency at the instance level. Since LIME uses local perturbations of input data, the stability of resulting explanations can vary based on the sampling distribution used to build the local surrogate model.

SHAP uses Shapley values from cooperative game theory to assign each feature an importance score based on all the combinations of features [6]. SHAP provides both local and global interpretability, which lets engineers find the most important elements that affect model predictions across the SSD fleet. SHAP provides more theoretically consistent feature attribution than LIME but is computationally expensive when applied to large datasets or complex ensemble models. Together, LIME and SHAP transform black-box SSD failure models into transparent, auditable systems that reliability teams can trust and validate.

In [11], the authors assess LIME and SHAP in the context of asset-failure prediction, differentiating between local and global explanation types and emphasizing the trade-offs between interpretability and model fidelity. In [12], the researchers evaluate multiple XAI techniques, including LIME and SHAP, in the context of hard disk drive (HDD) health prediction and report that SHAP yields more stable and comprehensive explanations. In [8], the authors developed a unified XAI framework that focuses on reliability, transparency, and making industrial systems easy for people to understand. Additional XAI techniques include Integrated Gradients which is a gradient-based attribution technique, along with global interpretation methods such as permutation feature importance and partial dependence analysis. Nonetheless, the systematic and operational-scale adoption of these explanatory techniques for predicting SSD failures in extensive data center environments is still limited, particularly under realistic temporal validation settings and large-scale telemetry datasets, highlighting a significant contribution of this research.

2.3. Machine Learning for SSD Failure Prediction

Earlier approaches used threshold-based monitoring of SMART attributes, but these methods didn't work well for capturing complex and non-linear degradation patterns observed in modern flash-based storage systems [4, 19, 20]. So, researchers have used data-driven machine-learning methods to create models of complicated failure dynamics using high-dimensional telemetry data [21]. Recent studies apply supervised machine-learning and deep learning to SSD failure prediction, leveraging SMART telemetry and large operational datasets. For example, in [2], the authors presented a comprehensive feature-selection framework that enhances failure prediction in diverse SSD deployments. In [18], the authors suggested a multiview random-forest methodology for elucidating failure modes and calculating time to failure. Ensemble methods such as Random Forest, Gradient Boosting, and XGBoost have proven highly effective in drive failure predictions, because of their ability to capture nonlinear relationships and intricate interactions

within SMART attribute telemetry [21].

Recent studies have also explored deep learning approaches like RNNs and temporal models to capture sequential patterns in storage telemetry data [22]. These models effectively capture complex temporal dependencies, but their limited interpretability limits their adoption in operational data centers, where engineers require a clear understanding of the factors driving predicted failures.

Besides supervised methods, many studies have explored unsupervised methods for predicting SSD failures. These techniques include anomaly detection, clustering, or probabilistic modeling to find unusual patterns of degradation without utilizing labeled failure data. In [23], the authors apply anomaly-detection models to SSD telemetry and show that unsupervised methods can uncover early warning signals that do not appear through basic threshold rules. In [24], the authors employ probabilistic and online-learning anomaly detectors to capture subtle temporal deviations in disk behaviour, highlighting the usefulness of label-free methods in operational environments. These unsupervised approaches complement supervised failure-prediction models by identifying emerging degradation trends that may precede labeled failure events.

While prior work such as [2], focuses on improving predictive performance through feature selection, our study emphasizes evaluating model behavior under realistic temporal validation and cost-sensitive deployment conditions, while integrating explainability techniques for operational transparency.

2.4. Cost-Sensitive Learning for SSD Failure Prediction

Failure prediction in data centers generally involves highly imbalanced datasets where failure events represent only a small fraction of all observations. In such cases, traditional accuracy-based evaluation metrics may be misleading because models can achieve high accuracy by simply predicting the majority class [21, 25].

To address this, researchers have explored cost-sensitive learning techniques that incorporate the relative cost of misclassification directly into the training or decision process. These approaches include weighted loss functions, cost-sensitive decision trees, and sampling-based strategies such as minority-class oversampling and other imbalance-handling techniques [21, 26]. These methods enable models to emphasize rare failure events without excessively biasing the model toward the dominant healthy-drive class.

In data centers, the cost of a false negative is typically much higher than the cost of a false positive. So, many disk failure prediction systems prioritize high recall to minimize the risk of unexpected drive outages that may lead to data loss or service disruption [18, 21]. Decision threshold optimization based on receiver operating characteristic (ROC) analysis, precision-recall evaluation, or cost-aware evaluation metrics has therefore become a common strategy for balancing failure detection performance with operational overhead in real-world deployments [18]. Most prior approaches incorporate cost sensitivity directly into model training through weighted loss functions or resampling strategies. In contrast, this study focuses on decision-level cost optimization via threshold tuning, allowing clearer interpretation of trade-offs between recall, false alarms, and

operational cost.

2.5. Probability Calibration and Decision Threshold Optimization

The reliability of probability estimates produced by models is an important consideration in operational decision systems. Well-calibrated probabilities ensure that predicted risk scores correspond to actual failure likelihoods, which is critical when predictions are used to guide maintenance scheduling or resource allocation [11, 12].

Several techniques have been proposed to improve probability calibration, including Platt scaling and isotonic regression, which are commonly used to adjust model outputs to better match observed event probabilities [26]. Calibration can also be evaluated using tools such as reliability diagrams and calibration curves, which compare predicted probabilities with observed outcome frequencies [26]. These calibration methods help ensure that decision thresholds correspond to meaningful operational risk levels. In predictive systems deployed in operational environments, calibrated probability estimates can support cost-aware decision-making by enabling organizations to select thresholds that minimize expected operational costs while maintaining acceptable failure detection rates [18, 21].

2.6. Research Gap and Motivation

Despite these advancements, there is still a significant gap in the operational deployment of SSD failure prediction. While supervised approaches, such as the feature-selection framework proposed by [2], achieve state-of-the-art performance, they often function as “black boxes”, limiting their transparency and interpretability. Recent work has begun to address this limitation. For instance, in [18], the authors utilized decision paths to explain failure modes in SSDs and [12] systematically compared LIME and SHAP for hard disk drive (HDD) failure prediction. Nevertheless, these studies mostly focus on improving engineering diagnostics, not the regulatory transparency and auditability requirements that new regulations like the EU AI Act [14] demand.

Furthermore, existing literature predominantly relies on standard performance metrics that fail to capture the asymmetric economic costs of maintenance decisions in data centers, where missing a failure is more costly than issuing a precautionary alert. This research uniquely addresses these gaps by proposing a compliance-ready framework that bridges high-performance prediction with rigorous interpretability mandates, while introducing a custom cost-sensitive evaluation strategy to validate the model’s operational viability.

3. Methodology

We formulate SSD failure prediction as a binary classification problem in which the objective is to predict whether an SSD will fail within a fixed 30-day prediction window.

Figure 1 shows the end-to-end machine-learning pipeline for SSD failure prediction with an Explainable AI (XAI) layer. Instead of using a random train-test split, we use a temporally defined training set, walk-forward validation, and a chronologically later holdout test set to better reflect real-world deployment conditions and prevent temporal data leakage.

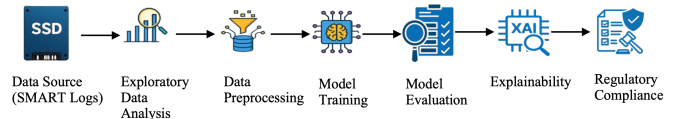


Figure 1: End-to-end architecture for SSD failure prediction with an explainability layer.

3.1. Data Ingestion

The first phase of the pipeline is Data Ingestion, in which SSD telemetry data (SMART logs) are collected daily at Alibaba from approximately 500,000 SSDs between January 2018 and December 2019. SMART attributes provide internal indicators of device health and are widely used in storage reliability and failure prediction research [18], [20]. Of these, 16,305 SSDs failed, while the remaining drives are considered healthy, resulting in a significant class imbalance with approximately 3% failure rate. The dataset has metadata columns (disk_id, model, ds) and SMART attributes (r_i, n_i). The r_i columns contain raw data, whereas the n_i columns contain normalized values for each attribute. In this study, we use the normalized SMART attributes (n_i) as predictive features, while metadata fields such as disk_id, model, ds, failure_time, and days_to_failure are used during preprocessing and labeling.

3.2. Exploratory Data Analysis

In the second phase, Exploratory Data Analysis (EDA), we looked at the differences in how healthy and failing drives behaved across six different SSD models using the temporally defined training set. Following the temporal split, we restricted this analysis to the training set to avoid leaking future data into feature selection and model design. Initial sparsity analysis indicated that 18 normalized SMART features had over 99.9% missing values and were therefore removed. For the remaining 33 normalized features, missing values were imputed with -1 to preserve the potential predictive signal of data sparsity. We intentionally used a sentinel value (-1) instead of statistical imputation so that the model could retain information about structural missingness, which may itself reflect vendor-specific SMART reporting behavior. We examined the Spearman rank correlation between normalized SMART attributes and the failure label (Failed) to identify the important indicators of degradation, as shown in Figure 2. Spearman correlation was selected because it captures monotonic relationships between SMART features and failure events without assuming linear dependencies.

Spearman Correlation Matrix: Normalized SMART Features and 'Failed' Label (Training Set)

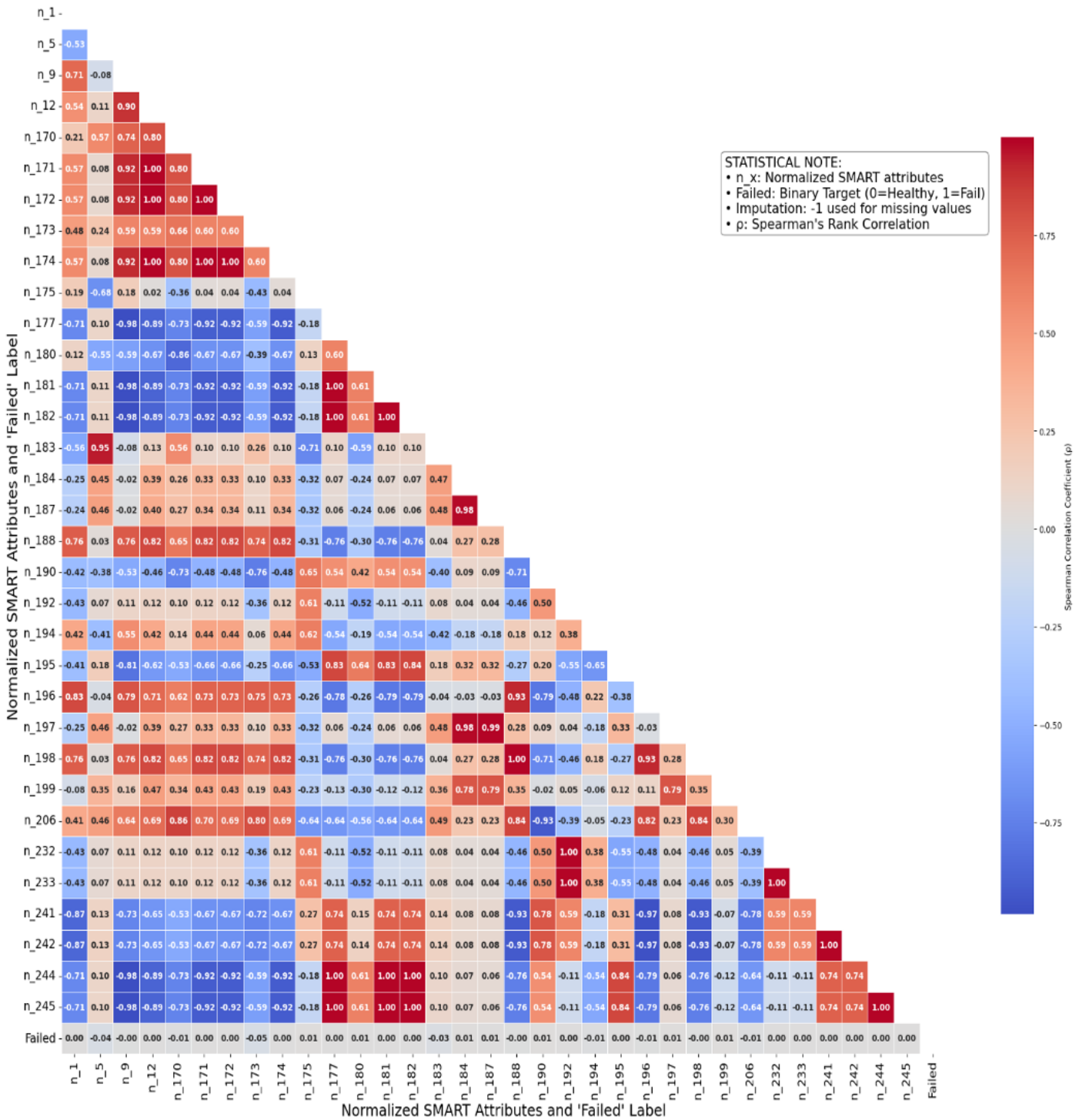


Figure 2: Spearman correlation matrix of selected normalized SMART attributes and the "Failed" label.

Beyond direct target correlation, we examined the full feature-to-feature correlation matrix to detect multicollinearity. Our analysis revealed significant multicollinearity, with 32 redundant feature pairs having absolute Spearman correlation coefficients greater than or equal to 0.95. These correlations formed seven clusters of highly related features. Instead of applying automated feature elimination, we cross-referenced these clusters with SMART attribute definitions and retained the most operationally meaningful feature within each cluster. This

cluster-based selection procedure reduced the 33 features to 17 SMART attributes while preserving the most informative degradation signals and minimizing redundancy. The final retained feature set consisted of the following 17 normalized SMART attributes: n_1, n_5, n_9, n_170, n_173, n_174, n_175, n_180, n_190, n_194, n_195, n_196, n_197, n_198, n_199, n_206, and n_232. A detailed description of the correlation clusters and the domain-informed feature selection process is provided in Appendix A.

3.3. Data Preprocessing

We built a preprocessing pipeline to transform the raw telemetry into a robust training set. This pipeline addressed issues related to time, class imbalance, and high dimensionality:

- Temporal Filtering and Integrity:** To ensure sufficient historical context, we removed all SSDs (both healthy and failed) with fewer than 30 days of operational records. Additionally, for failed drives specifically, if data gaps exceeded 30 consecutive days, we discarded records following the gap and treated the last available record as the failure date to maintain causal integrity. We created a composite key (disk_id, model) to prevent data from getting mixed up between different SSD models because disk_id is not unique across models. After this step, the dataset retained records from 101,509 unique SSDs, consisting of 16,008 failed drives and 85,501 healthy drives.
- Predictive Labeling:** We created a binary target variable called "Failed" for all the SSDs by utilizing a fixed prediction window. Records that were seen within 30 days prior to a failure event were given a 1 (positive) label, while all records that came before that and all records from healthy drives were given a 0 (negative) label. At record level, the labeling process created 454,936 failed instances (Failed=1) and 54,960,816 healthy instances (Failed=0), representing 0.82% failure percentage.
- Temporal Train-Test Split:** We implemented a chronological data split to evaluate the model in a realistic deployment scenario. We identified a cut-off date (September 16, 2019), on or before which 80% of the drives failed. The 12,815 drives that failed on or before the cut-off date were reserved for the train set and 3,193 drives failed after the cut-off date were reserved for test set. The model-level distribution of failed drives is as follows:

Training set (12,815 failed drives): MA1 (1,354), MA2 (819), MB1 (1,458), MB2 (542), MC1 (7,663), and MC2 (979).

Test set (3,193 failed drives): MA1 (1), MA2 (38), MB1 (310), MB2 (50), MC1 (2,664), and MC2 (130).

To create a balanced training set, we included all records from each of the 12,815 failed drives in the training set. We then sampled an equal number of healthy drives (12,815) with the same model distribution as the failed drives in the training set. For these healthy drives, all the records between January 01, 2018, and September 16, 2019, were included in the training set. Records from these healthy drives after September 16, 2019, were excluded. This resulted in a balanced training dataset containing records from 25,630 drives and 10,637,778 observations. Table 1 shows the model-wise distribution of the balanced training set.

Table 1: Model-wise distribution of the balanced training set

Model	Healthy	Failed	Total
MA1	1354	1354	2708
MA2	819	819	1638
MB1	1458	1458	2916
MB2	542	542	1084
MC1	7663	7663	15326
MC2	979	979	1958

To create a realistic unbalanced test set, we retained records from 3,193 failed drives and 61,938 healthy drives. All drives in test set contain records between September 17, 2019, and December 31, 2019. So, in test set we have data from 65,131 unique drives and 5,499,337 observations. Table 2 shows the model-wise distribution of the unbalanced test dataset.

Table 2: Model-wise distribution of the unbalanced test set

Model	Healthy	Failed	Total
MA1	5877	1	5878
MA2	15214	38	15252
MB1	10084	310	10394
MB2	12505	50	12555
MC1	12454	2664	15118
MC2	5804	130	5934

- Feature Selection and Imputation:** We reduced dimensionality by removing raw SMART features (r_i) and only considering normalized features (n_i). We dropped 18 normalized attributes (n_i) that had more than 99.9% missing data. For the rest of the normalized attributes, we used a different category (-1) to impute the missing values. Finally, we used the Spearman correlation analysis from the EDA phase to get rid of 16 redundant features. This left us with a final feature set of 17 normalized SMART features.

3.4. Model Training

In the fourth phase, Model Training, we used the balanced training set produced during preprocessing to train three different tree-based ensemble models: Random Forest, XGBoost, and LightGBM. These algorithms were selected because tree-based ensembles are well suited to high-dimensional telemetry data and have demonstrated strong performance in prior storage failure prediction studies [2, 18].

We used a temporally balanced training set for model development. To perform hyperparameter tuning while retaining chronological order, we used fixed-date walk-forward validation on the training data. We defined three validation folds using temporal cutoffs on January 1, 2019, March 1, 2019, and May 1, 2019, with a 60-day validation window after each cutoff. To prevent drive-level leakage, any drive appearing in the training portion of a fold was excluded from the corresponding validation fold. This ensured both temporal integrity and drive-level isolation.

We used Randomized Search Cross-Validation to perform hyperparameter tuning for XGBoost, LightGBM, and

Random Forest. The search spaces for the evaluated hyperparameters are summarized in Table 3. Randomized search was performed using multiple parameter combinations with cross-validation on the temporally defined training set to identify configurations that maximize predictive performance while maintaining generalization. The final hyperparameter configurations selected for each model, cost ratio, and validation fold are reported in Table 4. Notably, the selected configurations were largely consistent across different cost ratios, indicating that performance variation is primarily driven by threshold optimization rather than substantial changes in model structure.

Based on cross-validation results and cost-sensitive evaluation, XGBoost was selected as the final model due to its superior performance in minimizing operational cost while maintaining high recall. The final model was retrained on the entire temporally defined training set using the most stable hyperparameter configuration observed across validation folds. Specifically, the configuration ($\text{max_depth} = 5$, $\text{learning_rate} = 0.1$, $\text{n_estimators} = 100$, $\text{min_child_weight} = 10$, $\text{gamma} = 0.2$, $\text{subsample} = 0.8$, $\text{colsample_bytree} = 0.8$, $\text{scale_pos_weight} \approx \text{IR}$) was consistently selected

across folds and cost ratios, indicating that performance is primarily driven by threshold optimization rather than structural changes in the model.

Table 3: Hyperparameter search space used in randomized search

Model	Hyperparameter	Search Space
XGBoost	max_depth	{3, 5, 7, 9}
	learning_rate	{0.01, 0.05, 0.1, 0.2}
	n_estimators	{100, 300, 500}
	min_child_weight	{1, 5, 10}
	gamma	{0, 0.1, 0.2}
	scale_pos_weight	{IR, 1.5×IR, 2×IR}
	subsample	{0.7, 0.8, 1.0}
	colsample_bytree	{0.7, 0.8, 1.0}
LightGBM	n_estimators	{100, 300, 500}
	learning_rate	{0.01, 0.05, 0.1}
	num_leaves	{31, 63, 127}
	scale_pos_weight	{IR, 1.5×IR}
Random Forest	n_estimators	{100, 300}
	max_depth	{5, 10, 20}
	min_samples_split	{2, 10}
	class_weight	{bal., bal._subsample}

IR: class imbalance ratio (healthy/failed samples)

Table 4: Final hyperparameters selected after randomized search

Model	Cost Ratio	Fold	Best Hyperparameters
XGBoost	10:1	1	subsample=0.8, scale_pos_weight=56.18, n_estimators=100, min_child_weight=10, max_depth=5, learning_rate=0.1, gamma=0.2, colsample_bytree=0.8
XGBoost	10:1	2	subsample=0.8, scale_pos_weight=56.18, n_estimators=100, min_child_weight=1, max_depth=3, learning_rate=0.01, gamma=0.1, colsample_bytree=0.8
XGBoost	10:1	3	subsample=0.8, scale_pos_weight=56.18, n_estimators=100, min_child_weight=10, max_depth=5, learning_rate=0.1, gamma=0.2, colsample_bytree=0.8
XGBoost	25:1	1-3	Same as 10:1 configuration
XGBoost	50:1	1-3	Same as 10:1 configuration
XGBoost	100:1	1-3	Same as 10:1 configuration
LightGBM	50:1	1	scale_pos_weight=28.09, num_leaves=31, n_estimators=500, learning_rate=0.01
LightGBM	50:1	2-3	scale_pos_weight=42.14, num_leaves=31, n_estimators=100, learning_rate=0.05
Random Forest	50:1	1-2	n_estimators=100, min_samples_split=2, max_depth=5, class_weight=balanced
Random Forest	50:1	3	n_estimators=100, min_samples_split=2, max_depth=10, class_weight=balanced, subsample

3.5. Model Evaluation

In the fifth phase, Model Evaluation, we went beyond standard statistical metrics to evaluate performance in a real-world operational context. We calculated Precision, Recall, F1-score, ROC-AUC, and PR-AUC, with a focus on Recall, false alarm rate (FAR), and cost-sensitive threshold performance because SSD failure prediction is a highly imbalanced classification problem [18, 21].

For each validation fold, the decision threshold was optimized over a range of candidate thresholds to minimize operational cost. We selected the final model using a custom Operational Cost Function. This function assigns a significantly higher cost to missed failures (False Negatives)

than to false alarms (False Positives). The total cost is calculated as:

$$\text{Total Cost} = FP \times 10 + FN \times 500 \quad (1)$$

Here, a False Negative (FN) incurs a \$500 penalty to reflect the risks of service disruption and data loss, while a False Positive (FP) incurs a \$10 cost for unnecessary inspection labor. The 50:1 cost ratio represents an illustrative operating scenario in which missing an impending failure is substantially more expensive than a precautionary inspection. To test the robustness of this assumption, we also conducted cost-sensitivity analysis across different false-negative to false-positive ratios of 10:1, 25:1, 50:1, and

100:1.

The final holdout test set was then used for one-time evaluation of the selected model after retraining on the full training data with the best hyperparameters.

3.6. Explainability and Regulatory Compliance

We incorporated a post-hoc explainability layer directly into the prediction pipeline to meet the transparency requirements discussed in Section 2.1. Specifically, we used LIME [5] to generate local surrogate models for each failure alert, enabling operators to interpret individual predictions by identifying the SMART attributes that contributed most to the decision. In parallel, SHAP values [6] were computed to provide a global view of feature importance and to verify that the model's decision patterns align with known physical degradation signals rather than spurious correlations. Unlike prior work that primarily applies explainability for diagnostic interpretation, our approach integrates these methods within an operational monitoring pipeline to support auditability and decision transparency in production environments.

In addition to interpretability, we analyzed model behavior at both global and local levels using SHAP and LIME, respectively. While SHAP provided a dataset-level view of feature importance, LIME enabled instance-level inspection of individual predictions, allowing us to validate that the model's decisions are consistent with known SSD degradation characteristics. This dual-level explanation supports both system-level and instance-level validation, which are essential for compliance with AI governance requirements. Furthermore, this framework transforms opaque probability scores into interpretable insights that can be independently verified, directly supporting transparency standards defined by frameworks such as the NIST AI Risk Management Framework [15].

3.7. Data and Code Availability

The original SSD dataset used in this study is publicly available as part of the Alibaba DCBrain SSD SMART logs repository:

https://github.com/alibaba-edu/dcbrain/tree/master/ssd_smart_logs

The code used for data preprocessing, model training, cost-sensitive evaluation, calibration analysis, ablation study, per-model analysis, and explainability analysis is publicly available at:

https://github.com/sauravintheocean/SSD_Failure_Prediction_XAI

Due to the large size of the dataset, the processed data is not distributed directly. However, the repository includes all necessary scripts and documentation to reconstruct the

processed dataset and reproduce the results reported in this paper.

4. Results and Analysis

In this section, we present the experimental results of our study, focusing on predictive performance, operational cost, and explainability under the temporal validation framework described in Section 3.

First, we analyze the sensitivity of the XGBoost model to different false-negative to false-positive cost ratios (10:1, 25:1, 50:1, and 100:1). This analysis evaluates how the optimal decision threshold and model performance vary under different cost assumptions, with the goal of identifying an appropriate operating regime for failure prediction. Based on this analysis, the 50:1 cost ratio was selected as the most suitable trade-off between minimizing total operational cost and maximizing recall of impending failures.

Second, we compare the performance of Random Forest, XGBoost, and LightGBM using walk-forward validation under the selected 50:1 cost ratio.

Finally, we report the performance of the final retrained XGBoost model on the chronologically later holdout test set and assess its transparency using SHAP and LIME.

4.1. Cost Sensitivity Analysis of XGBoost

Table 5 reports the mean and standard deviation across the three temporal validation folds. As the cost ratio increased from 10:1 to 50:1, the mean recall of XGBoost increased from $44.69\% \pm 48.11\%$ to $70.83\% \pm 50.52\%$, while the mean false alarm rate increased from 0.3595 ± 0.5553 to 0.6686 ± 0.5674 . The optimal average threshold decreased from 0.4700 ± 0.3984 at lower cost ratios to 0.3114 ± 0.3532 at higher ratios, indicating that the observed changes are primarily driven by threshold adjustment rather than substantial changes in model structure.

Although variability across folds is substantial, this is largely due to the highly uneven number of failure cases in the validation windows. The fold-level results should therefore be interpreted as an exploratory sensitivity analysis rather than as a definitive estimate of deployment variance.

Increasing the cost ratio beyond 50:1 did not lead to improvements in recall, precision, or ranking performance. As shown in Table 5, the performance metrics at 50:1 and 100:1 are identical, while the mean operational cost increases from \$30,720 to \$31,886.67. This indicates that the model has reached its maximum achievable recall under the given feature space and temporal validation setup. Therefore, the 50:1 ratio represents the most cost-effective operating point, achieving the same detection performance as higher ratios while avoiding unnecessary increases in operational cost.

Table 5: XGBoost Cost-Sensitivity Analysis Across Temporal Validation Folds

Cost Ratio (FN:FP)	Cost (\$)	Recall	Precision	FAR	PR-AUC	ROC-AUC	Threshold
10:1	14,107 ± 11,476	44.69% ± 48.11%	7.36% ± 3.21%	0.36 ± 0.56	0.05 ± 0.03	0.49 ± 0.12	0.47 ± 0.40
25:1	21,907 ± 19,791	44.69% ± 48.11%	7.36% ± 3.21%	0.36 ± 0.56	0.05 ± 0.03	0.49 ± 0.12	0.47 ± 0.40
50:1	30,720 ± 32,135	70.83% ± 50.52%	5.41% ± 3.78%	0.67 ± 0.57	0.05 ± 0.03	0.49 ± 0.12	0.31 ± 0.35
100:1	31,887 ± 30,698	70.83% ± 50.52%	5.41% ± 3.78%	0.67 ± 0.57	0.05 ± 0.03	0.49 ± 0.12	0.31 ± 0.35

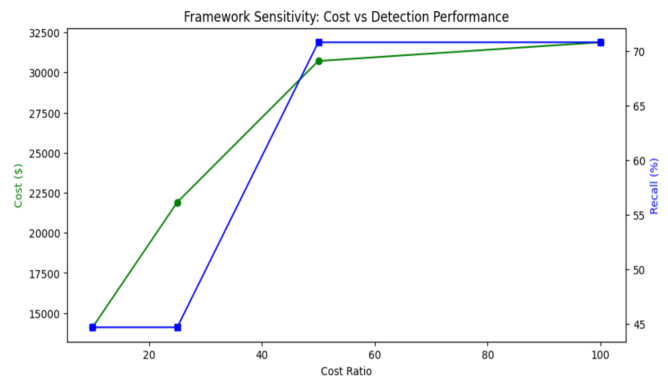


Figure 3: Sensitivity of operational cost and recall to different cost ratios. Figure 3 illustrates the sensitivity of the final XGBoost model to varying cost ratios. As the cost ratio increases, the model prioritizes higher recall, resulting in more aggressive failure detection at the expense of increased false alarms. This behavior highlights the trade-off between minimizing missed failures and controlling operational overhead in real-world data center environments.

4.2. Model Comparison at 50:1 Cost Ratio

We compared the performance of XGBoost, LightGBM, and Random Forest at a 50:1 cost ratio using walk-forward temporal validation. Table 7 reports the mean and standard deviation across the three validation folds.

All three models achieved identical mean recall (70.83% \pm 50.52%), indicating that under aggressive cost-sensitive thresholding, each model prioritizes maximizing failure detection. However, differences emerge in ranking performance and stability. LightGBM achieved the highest ROC-AUC (0.5738 \pm 0.1938), followed by XGBoost and Random Forest. Additionally, XGBoost achieved slightly lower false alarm rates and competitive precision compared to both baselines.

Despite these differences, overall performance across models remains highly similar. The large standard deviations observed across all metrics are primarily due to the uneven distribution of failure cases across validation folds, particularly the presence of folds with very few failure instances.

To further assess whether the observed differences are statistically significant, we conducted paired t-tests and Wilcoxon signed-rank tests using fold-level results. As shown in Table 6, no statistically significant differences were observed between XGBoost and the baseline models for cost, recall, precision, FAR, PR-AUC, or F1-score ($p > 0.05$). A statistically significant difference was observed only for ROC-AUC between XGBoost and Random Forest ($p = 0.025$), indicating improved ranking performance for XGBoost in this specific comparison.

Table 6: Statistical Significance Tests (XGBoost vs Baselines, 50:1)

Comparison	Metric	p-value	Significance
XGBoost vs LightGBM	Cost	0.465	Not significant
XGBoost vs LightGBM	Recall	-	Identical
XGBoost vs LightGBM	Precision	0.856	Not significant
XGBoost vs LightGBM	FAR	0.557	Not significant
XGBoost vs LightGBM	PR-AUC	0.232	Not significant
XGBoost vs LightGBM	ROC-AUC	0.307	Not significant
XGBoost vs LightGBM	F1	0.809	Not significant
XGBoost vs Random Forest	Cost	0.423	Not significant
XGBoost vs Random Forest	Recall	-	Identical
XGBoost vs Random Forest	Precision	0.423	Not significant
XGBoost vs Random Forest	FAR	0.423	Not significant
XGBoost vs Random Forest	PR-AUC	0.826	Not significant
XGBoost vs Random Forest	ROC-AUC	0.025	Significant
XGBoost vs Random Forest	F1	0.423	Not significant

These results indicate that all three models perform comparably under cost-sensitive thresholding, with most performance differences not statistically significant. While XGBoost demonstrates competitive performance and slightly improved ranking behavior in specific comparisons, the results suggest that model choice has a limited impact relative to threshold optimization in this setting.

4.3. Final Model Evaluation on Holdout Test Set

We retrained the XGBoost model on the complete training dataset using the optimal hyperparameters identified in Section 3.4 at the selected 50:1 cost ratio. The final model was evaluated on a chronologically later holdout test set to simulate real-world deployment conditions. Instead of using a fixed classification threshold, we performed a threshold sweep on the holdout set to identify the operating point that maximizes economic benefit. The optimal threshold was found to be 0.68, which balances missed failures and false alarms under the defined cost structure. Table 8 shows the performance of XGBoost on the holdout test set.

Table 8: Final model performance on holdout test set

Metric	Value
Cost Ratio (FN: FP)	50:1
Optimal Threshold	0.68
Net Operational Savings	\$13,419,280
Recall	67.98%
Precision	4.43%
F1-score	0.083
FAR	0.1878
PR-AUC	0.0386
ROC-AUC	0.7625
TP	47,236
FP	1,019,872
FN	22,250
TN	4,409,979

The model successfully identified 67.98% of impending failures while maintaining a manageable false alarm rate (FAR = 0.1878). Although precision remains low (4.43%), this behavior is expected in highly imbalanced failure prediction tasks where maximizing recall is critical. The higher ROC-AUC observed on the holdout test set compared to validation folds is primarily due to the larger number of failure instances, resulting in a more stable and representative estimate of ranking performance.

From an operational perspective, the model generated approximately 22.6 alerts per true failure, reflecting the trade-off between proactive failure detection and inspection overhead. Despite this, the optimized strategy yields a substantial net operational savings of \$13.4 million, demonstrating the economic value of cost-sensitive learning in data center environments.

While the proposed model achieves significant reductions in missed failures, it generates many false alarms (approximately 1.02 million in the holdout period). In practice, data centers do not manually inspect every flagged drive. Instead, alerts are typically integrated into automated monitoring pipelines and prioritized using additional operational heuristics.

First, alerts can be ranked by predicted failure probability, allowing operators to focus only on the top- k % highest-risk drives. This prioritization can substantially reduce inspection overhead while still capturing a large proportion of true failures.

Table 7: Model Comparison at 50:1 Cost Ratio (Mean \pm SD)

Model	Cost (\$)	Recall	Precision	FAR	PR-AUC	ROC-AUC	Threshold
XGBoost	30,720 \pm 32,135	70.83% \pm 50.52%	5.41% \pm 3.78%	0.67 \pm 0.57	0.05 \pm 0.03	0.49 \pm 0.12	0.31 \pm 0.35
LightGBM	30,763 \pm 32,214	70.83% \pm 50.52%	5.41% \pm 3.79%	0.67 \pm 0.57	0.05 \pm 0.04	0.57 \pm 0.19	0.33 \pm 0.28
Random Forest	30,886 \pm 32,412	70.83% \pm 50.52%	5.41% \pm 3.79%	0.67 \pm 0.57	0.05 \pm 0.04	0.44 \pm 0.11	0.31 \pm 0.3

Second, many false positives correspond to drives exhibiting early signs of degradation that may not immediately fail but still warrant closer monitoring. As a result, these alerts are not necessarily wasted effort but can contribute to preventive maintenance strategies.

Third, inspection in modern data centers is often partially automated, involving background diagnostics, SMART log analysis, or scheduled maintenance cycles rather than manual intervention for each alert. Therefore, the reported number of false alarms should be interpreted as an upper bound under a fully reactive scenario. In practice, alert prioritization, batching, and automation significantly reduce the effective operational burden.

4.4. Ablation Study

To quantify the contribution of different feature groups, we conducted an ablation study by systematically removing key categories of SMART attributes, including wear indicators, temperature-related features, and error metrics. The results are summarized in Table 9.

Removing wear-related features (n_{173} and n_{180}) resulted in a dramatic performance degradation, with recall dropping from 67.98% to 7.85% and F1-score decreasing from 0.083 to 0.017. This confirms that wear-level indicators are the dominant predictors of SSD failure and are critical for reliable detection.

In contrast, removing temperature-related features (n_{190} and n_{194}) led to a moderate reduction in recall (67.98% to 61.05%), indicating that thermal signals provide complementary information that improves model robustness but are not the primary drivers of prediction.

Finally, removing error-related features had minimal impact on recall but slightly reduced precision and increased the false alarm rate, suggesting that these features contribute marginally to decision refinement but are less informative than wear and temperature indicators.

Overall, the ablation results are consistent with the SHAP analysis and demonstrate that the model's predictions are grounded in physically meaningful degradation signals rather than spurious correlations. All ablation experiments were conducted on the holdout test set using the fixed optimal threshold ($T = 0.68$) to ensure fair comparison.

Table 9: Ablation Study Results

Experiment	Recall	Precision	F1	FAR
Full Model	67.98%	4.43%	0.083	0.1878
No Wear	7.85%	0.98%	0.017	0.1017
No Temp	61.05%	4.54%	0.084	0.1643
No Error	68.97%	4.16%	0.084	0.2036

4.5. Calibration Analysis

To evaluate the reliability of predicted probabilities, we assessed model calibration using a reliability diagram,

calibration table, and Brier score on the holdout test set. As shown in Figure 4, the reliability curve lies consistently below the diagonal, indicating that predicted probabilities systematically overestimate the true failure likelihood, particularly at higher probability ranges. The calibration was evaluated post hoc and was not explicitly optimized during model training.

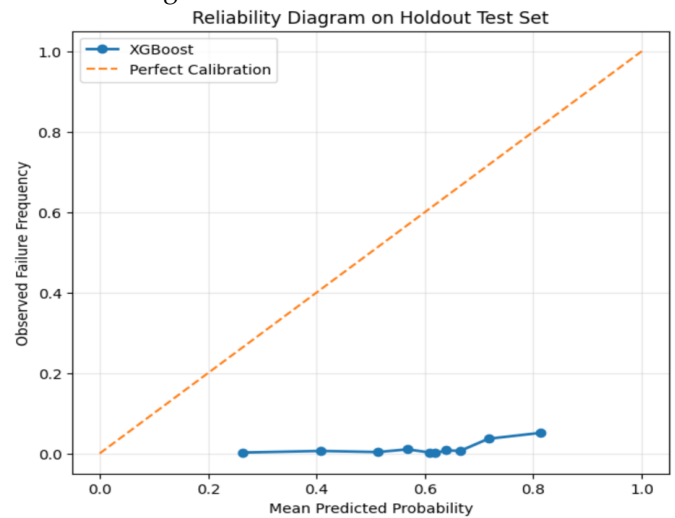


Figure 4: Reliability Diagram on Holdout Test Set

This trend is further supported by the calibration table (Table 10), where observed failure frequencies remain significantly lower than predicted probabilities across all bins.

Table 10: Calibration Table

Predicted Probability Bin	Observed Frequency
0.265	0.0024
0.408	0.0062
0.514	0.0036
0.568	0.0102
0.608	0.0026
0.619	0.0008
0.639	0.0078
0.665	0.0061
0.717	0.0365
0.814	0.0513

The Brier score of 0.3547 indicates limited probability calibration, which is expected given the extreme class imbalance and the cost-sensitive optimization strategy employed in this work. The model is explicitly optimized to maximize recall and economic utility rather than to produce well-calibrated probability estimates.

Despite this, threshold-based decision making remains effective, as the framework relies on relative risk ranking rather than absolute probability accuracy. The optimal operating threshold is determined empirically through cost optimization, ensuring robust operational performance even in the presence of calibration error.

Despite calibration limitations, the model maintains strong ranking performance (ROC-AUC = 0.7625), indicating reliable relative risk ordering. Future work may explore post-hoc calibration techniques such as Platt scaling or iso-

tonic regression to improve probability reliability without compromising cost-sensitive performance.

4.6. Baseline Comparison (Walk-Forward Validation)

To further evaluate the effectiveness of the proposed framework, we compared its performance against three additional baseline approaches: (1) Logistic Regression, (2) a heuristic top- k model based on wear-level indicators, and (3) a feature-reduced XGBoost model inspired by prior work. All models were evaluated using the same walk-forward temporal validation and cost-sensitive optimization framework (50:1 cost ratio). The results are summarized in Table 12.

Logistic Regression achieves high recall in some folds but only by significantly increasing the false alarm rate, indicating poor discrimination capability under extreme class imbalance. In contrast, the heuristic top- k baseline demonstrates limited predictive power, with substantially lower recall and higher operational cost, confirming that simple threshold-based rules are insufficient for SSD failure prediction. The feature-reduced XGBoost baseline performs better than the heuristic model but exhibits instability across folds.

However, all baseline models failed to detect failures in Fold 2, where only eight failure events were present. Under such extreme sparsity, cost minimization favors conservative thresholds, leading to zero recall. This highlights the sensitivity of simpler models to rare-event scenarios.

Finally, these results indicate that accurate SSD failure prediction requires modeling complex, multi-dimensional feature interactions. Simplified models and heuristic approaches are insufficient for capturing the underlying failure dynamics in hyperscale environments.

4.7. Final Holdout Comparison

We compared the performance of the proposed XGBoost model against the strongest baseline models on an independent holdout test set. Logistic Regression and the feature-reduced XGBoost model were selected based on their performance in the walk-forward validation stage. The results are summarized in Table 13.

Logistic Regression has extremely low recall (0.7%), failing to detect most failures despite maintaining a low false alarm rate. This indicates that linear models are insufficient for capturing the complex, non-linear degradation patterns present in SSD data.

The feature-reduced Xu-style XGBoost achieves the highest recall (72.67%) and lowest operational cost (\$18.51M), resulting in the highest net savings (\$16.24M). It also produces fewer alerts per true failure (18.8), indicating improved operational efficiency. This improvement is due to focusing on a subset of highly predictive SMART attributes, reducing noise from less informative features. However, this simplified model demonstrates reduced robustness, as evidenced by its instability during walk-forward validation.

The full-feature XGBoost model achieves slightly lower recall (67.98%) and higher operational cost but demonstrates more stable performance across temporal validation (Section 4.6). These results highlight an important trade-off

between model simplicity and robustness. While feature reduction can improve performance on specific datasets, the proposed framework prioritizes consistent, cost-sensitive performance across diverse operating conditions.

4.8. Per-Model Performance Analysis

To evaluate model generalization across different hardware types, we analyzed performance separately for each SSD model on the holdout test set. The results are summarized in Table 11.

Table 11: Per-Model Performance Analysis

Model	Samples	Recall	Precision	FAR
MA1	481,617	8.00%	0.01%	0.0340
MA2	1,252,002	6.73%	0.12%	0.0422
MB1	927,930	29.22%	1.73%	0.1323
MB2	1,127,559	7.69%	0.08%	0.1063
MC1	1,189,688	74.53%	7.06%	0.4945
MC2	520,541	81.66%	1.57%	0.2878

The model demonstrates substantial variation in predictive performance across SSD models. For example, MC2 and MC1 exhibit strong recall (81.66% and 74.53%, respectively), indicating that failure patterns for these models are well captured by the learned feature space. In contrast, other models such as MA1, MB2, and MA2 show significantly lower recall (below 10%), suggesting that their failure signatures are either less pronounced or not fully represented by the available SMART attributes.

This variability highlights the heterogeneous nature of SSD failure mechanisms across different hardware models. Some devices exhibit clear degradation patterns (e.g., wear-out behavior), while others may fail due to more stochastic or unobserved factors, making prediction inherently more challenging. Despite these differences, high-performing models contribute significantly to overall cost savings. From an operational perspective, this suggests that model deployment can be further optimized by incorporating model-specific thresholds or training specialized models per device family.

These findings emphasize the importance of hardware-aware modeling strategies and motivate future work on domain adaptation and per-device calibration techniques. This result further reinforces that global performance metrics may mask significant variability across hardware types.

4.9. Explainability Analysis

To ensure the model's decisions are transparent and trustworthy for data center operators, we applied SHAP for global feature analysis and LIME for individual failure auditing.

Table 12: Baseline Comparison at 50:1 Cost Ratio (Mean ± SD)

Model	Cost (\$)	Recall	Precision	FAR	PR-AUC	ROC-AUC	Threshold
Logistic Regression	26,920 ± 25,946	66.67% ± 57.7%	4.42% ± 5.05%	0.60 ± 0.53	0.09 ± 0.11	0.52 ± 0.26	0.37 ± 0.34
Heuristic Top- <i>k</i>	44,233 ± 40,508	33.07% ± 39.3%	4.74% ± 5.43%	0.29 ± 0.36	0.09 ± 0.13	0.51 ± 0.18	0.30 ± 0.36
Xu-style XGBoost	30,310 ± 31,531	66.67% ± 57.7%	4.25% ± 5.12%	0.65 ± 0.56	0.09 ± 0.11	0.52 ± 0.17	0.42 ± 0.20

Table 13: Final Holdout Comparison (50:1)

Model	Thr	Savings (\$)	Cost (\$)	Recall	Prec	F1	FAR	PR-AUC	ROC-AUC	Alerts/Fail
XGBoost (Full)	0.68	13.4M	21.32M	67.98%	4.43%	0.083	0.188	0.039	0.7625	22.6
Logistic Regression	0.85	0.11M	34.63M	0.70%	3.61%	0.0117	0.002	0.015	0.582	27.7
Xu-style XGBoost	0.53	16.2M	18.51M	72.67%	5.31%	0.0989	0.166	0.044	0.768	18.8

Global Feature Importance (SHAP)

Features are ranked by their mean absolute SHAP value, with color representing the feature value (red = high, blue = low). As shown in Figure 5, *n*₁₇₃ (Wear Leveling Count) emerges as the most important feature. Lower values of *n*₁₇₃ (blue points) are strongly associated with positive SHAP values, indicating higher failure risk. This behavior is consistent with the physical interpretation of wear leveling, where lower values of the normalized wear-leveling count indicate progressive exhaustion of SSD endurance.

In addition, *n*₁₉₀ (Airflow Temperature / thermal variation indicator), *n*₉ (Power-On Hours), *n*₁₉₄ (Temperature), and *n*₁₈₀ (Unused Reserved Block Count) also contribute to the model’s predictions, capturing complementary signals related to device aging, thermal stress, and available spare capacity. The SHAP distributions show consistent directional patterns across these features, where variations in feature values correspond to predictable changes in failure risk.

This indicates that the XGBoost model is learning meaningful hardware-level signals rather than spurious correlations, supporting its reliability for real-world deployment.

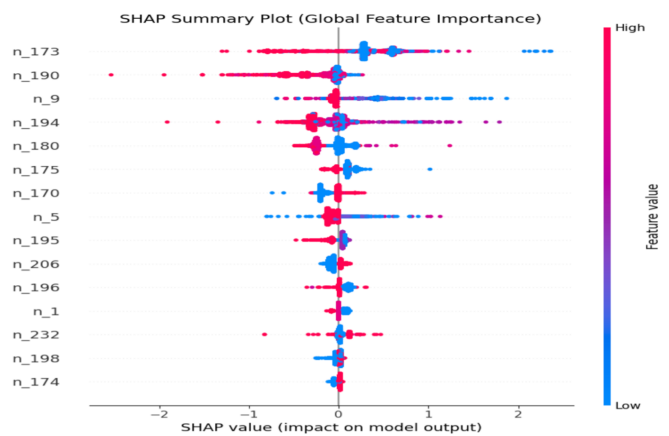


Figure 5: SHAP Summary Plot (Global Feature Importance)

Local Failure Diagnosis (LIME)

We used LIME analysis to audit individual predictions, which gave us detailed information about each prediction.

Figure 6 illustrates a True Positive prediction for a failed drive. The LIME explanation shows that *n*₁₇₃ (Wear Leveling Count) is the dominant contributor, where very low values strongly push the prediction toward failure. Additional contributing factors include *n*₁₈₀ (Unused Reserved Block Count) and imputed values such as *n*₂₃₂ ≤ -1, indicating potential degradation or missing telemetry sig-

nals associated with increased failure risk. These features collectively reinforce the model’s ability to detect drives nearing end-of-life conditions.

Conversely, Figure 7 presents a True Negative prediction for a healthy drive. In this case, high values of *n*₁₇₃ (Wear Leveling Count) are the primary contributors toward a healthy classification, indicating sufficient remaining endurance. Additional positive contributions from *n*₁₉₀ (thermal indicator) and *n*₁₉₄ (temperature) further support the healthy prediction. While some features (e.g., imputed or weak degradation signals) push slightly toward failure, their influence is outweighed by stronger indicators of normal operating conditions.

These instance-level explanations demonstrate that the model’s predictions are driven by coherent and interpretable feature interactions, consistent with known physical behavior of SSD degradation and operational conditions.

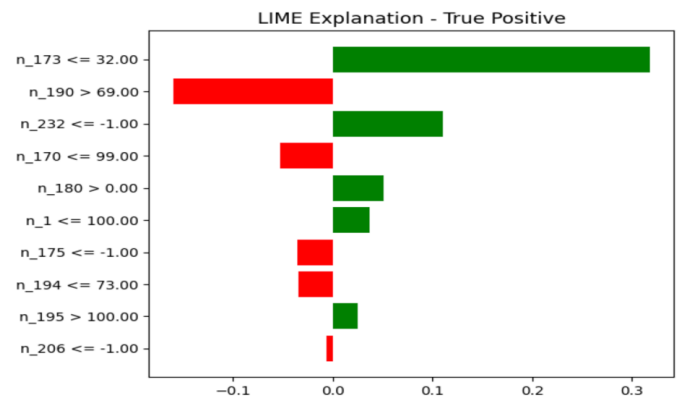


Figure 6: LIME Explanation for a True Positive Prediction

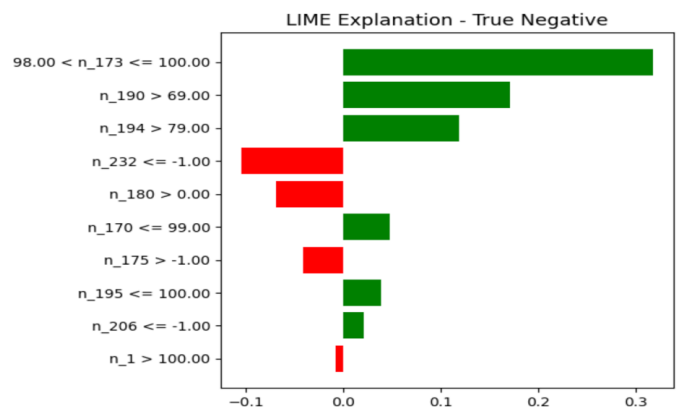


Figure 7: LIME Explanation for a True Negative Prediction

5. Discussion

In this section, we interpret the experimental results within the broader context of data center operations. Beyond standard performance metrics, we analyze the operational feasibility of the proposed framework, justify the economic trade-offs inherent in the “Safety-First” strategy, and discuss the long-term reliability implications for hyperscale storage fleets.

5.1. Implications for Data Center Operations

The results show that under cost-sensitive thresholding, all three models (XGBoost, LightGBM, and Random Forest) converge to similar operating characteristics, achieving comparable recall (~70%) and cost performance. This indicates that threshold optimization plays a more significant role than model architecture in highly imbalanced failure prediction settings.

Despite similar aggregate performance, XGBoost was selected as the final model due to its consistent behavior across validation folds, competitive false alarm rates, and strong interpretability properties. The SHAP and LIME analyses further confirm that its predictions are driven by physically meaningful signals, making it more suitable for operational deployment.

From an operational perspective, the proposed framework functions as a high-sensitivity screening system rather than an autonomous decision-maker. The deployment workflow follows a two-stage process:

- The model flags drives exhibiting anomalous behavior (e.g., degradation in wear-leveling count or abnormal thermal patterns).
- Flagged drives are subjected to lightweight diagnostics, SMART log inspection, or scheduled maintenance review.

This hierarchical approach ensures that false alarms incur low marginal cost, while significantly reducing the risk of catastrophic failures. As a result, the system enables a transition from reactive to proactive maintenance strategies in large-scale storage environments.

An important observation from the baseline comparison is the trade-off between model simplicity and robustness. While the feature-reduced Xu-style XGBoost achieves higher recall and lower cost on the holdout set, it exhibits instability across temporal validation folds. In contrast, the full-feature XGBoost model provides more consistent performance, highlighting the importance of robustness in real-world deployment scenarios.

5.2. Economic Impact and Cost Asymmetry

The primary driver of this study is the asymmetric nature of failure costs. Missing a failure (false negative) can lead to severe consequences, including data loss and service disruption, while false alarms primarily incur inspection costs. Through cost-sensitivity analysis (Section 4.1), we observed that increasing the FN:FP ratio shifts the model toward higher recall at the expense of increased false alarms. Performance stabilizes beyond a 50:1 ratio, where further

increases do not improve recall or ranking metrics but lead to higher operational cost. This identifies 50:1 as the most cost-effective operating point.

On the holdout test set, the optimized model achieved \$13.4 million in net operational savings, demonstrating the economic value of cost-aware threshold selection. This highlights a key insight: in hyperscale environments, optimal decision-making is driven by economic objectives rather than traditional classification metrics.

5.3. The Strategic Importance of Low Precision

A key finding of this study is that low precision (~4.4%) is not a limitation but a deliberate design choice under asymmetric cost conditions. In conventional classification tasks, low precision is undesirable. However, in failure prediction:

- Missing failures is extremely costly
- False alarms are relatively inexpensive

Thus, maximizing precision would require stricter thresholds, significantly reducing recall and increasing the risk of undetected failures. Instead, the proposed framework adopts a “Safety-First” strategy, prioritizing recall to ensure that most at-risk drives are identified.

Importantly, the explainability analysis confirms that false positives are not random noise; rather, they often correspond to drives exhibiting early warning signals such as thermal stress or wear degradation.

These drives, although not immediately failing, represent latent risk, making their identification operationally valuable. Consequently, the model functions as a preventive screening mechanism, balancing reliability and operational cost.

5.4. Managing False Alarms

A practical challenge in deployment is the high number of false alarms (approximately 1.02 million in the holdout period). However, in real-world data center environments, not all alerts are treated equally.

The following strategies help mitigate this burden:

- **Risk-based prioritization:** Alerts can be ranked by predicted failure probability, allowing operators to focus on the highest-risk subset (e.g., top 5–10%).
- **Batching and automation:** Many diagnostics are automated through SMART monitoring tools, reducing manual inspection effort.
- **Preventive maintenance value:** Some false positives correspond to drives under stress that may fail soon, providing early intervention opportunities.

Therefore, the reported false alarm count represents a worst-case upper bound, while the effective operational burden is significantly lower in practice.

5.5. Limitations and Future Directions

This research highlights several limitations inherent to the current methodology:

- **Temporal Resolution:** The current analysis relies on daily snapshots of SMART attributes. While this frequency works well for capturing slow degradation (e.g., wear leveling), it makes it difficult to detect rapid-onset failures, which are catastrophic breakdowns that occur within the 24-hour interval between status updates (e.g., mechanical shock or controller failure).
- **Dataset Specificity:** The Alibaba dataset is large and comprehensive but represents a specific operating environment with distinct workload and cooling characteristics. As a result, the model's applicability to other hyperscale data centers or storage fleets with different drive manufacturers and model generations requires additional validation.
- **Cost Model Simplification:** Although we conducted sensitivity analysis across four false-negative to false-positive cost ratios (10:1, 25:1, 50:1, and 100:1), these scenarios remain predefined and illustrative. In operational settings, the true cost of missed failures and false alarms may vary dynamically depending on data criticality, drive type, service-level requirements, and replacement logistics.
- **Explainability vs. Causality:** SHAP and LIME identify correlations (e.g., high temperature correlates with failure), but they do not establish causation. It remains unclear whether elevated temperature causes failure or whether a failing component generates excess heat.

Based on these limitations, we propose the following avenues for future research:

- **Integration of Time-Series Deep Learning Models:** Moving from static classifiers such as XGBoost to sequence-based models (e.g., Long Short-Term Memory (LSTM) networks or Transformers) enables explicit modeling of temporal dynamics in SMART attributes, potentially improving the detection of rapid degradation events.
- **Heterogeneous Fleet Validation:** Extending the framework to include Hard Disk Drives (HDDs). Mechanical storage exhibits fundamentally different failure modes than flash-based SSDs (e.g., motor vibration vs. NAND wear), requiring distinct feature engineering and failure signatures to ensure generalization across mixed data center fleets.
- **Dynamic Cost Functions:** Developing adaptive thresholding systems that adjust decision boundaries in real time based on data criticality and replacement cost, rather than relying on fixed global constants.
- **Human-in-the-Loop Evaluation:** Conducting field studies with data center technicians to evaluate the interpretability and actionability of LIME explanations. Feedback from domain experts is essential to refining risk visualization and ensuring that model outputs are trustworthy and actionable.

6. Conclusion

This study demonstrates that effective predictive maintenance in hyperscale data centers requires moving beyond standard accuracy metrics toward cost-sensitive and explainable AI frameworks. Using the Alibaba SSD dataset, we addressed the extreme class imbalance in failure prediction by combining cost-aware threshold optimization with interpretable modeling techniques.

Our results show that model performance in this setting is driven less by algorithmic differences and more by cost-sensitive threshold selection. Through systematic sensitivity analysis across multiple cost ratios (10:1, 25:1, 50:1, and 100:1), we identified 50:1 as the most cost-effective operating point, beyond which no further improvements in recall or ranking performance were observed.

On a chronologically separated holdout test set, the optimized XGBoost model achieved 67.98% recall and generated approximately \$13.4 million in net operational savings, demonstrating the practical value of a "Safety-First" strategy that prioritizes failure detection over precision. While this approach results in a higher number of false alarms, we show that these can be effectively managed through prioritization, automation, and staged inspection workflows, making the framework operationally feasible.

Importantly, the integration of SHAP and LIME ensures that model predictions are transparent and physically interpretable, with key features such as wear leveling, thermal indicators, and device age aligning with known hardware degradation mechanisms. This interpretability is critical for building trust and enabling adoption in real-world data center environments.

Although the proposed framework demonstrates strong performance, it remains subject to limitations related to dataset specificity, temporal resolution, and simplified cost modeling. Future work should focus on extending the approach to time-series deep learning models, validating across heterogeneous storage fleets, and incorporating adaptive, context-aware cost functions.

Ultimately, this research bridges the gap between predictive modeling and operational deployment. By aligning machine learning objectives with economic realities and providing interpretable decision support, the proposed framework offers a scalable solution for reliability management not only in data centers but also in other critical infrastructure domains where failure costs are asymmetric and transparency is essential.

References

- [1] D. Reinsel, J. Gantz, J. Rydning, "The digitization of the world from edge to core", Tech. Rep. US44413318, IDC, 2018.
- [2] F. Xu, S. Han, P. P. C. Lee, Y. Liu, C. He, J. Liu, "General feature selection for failure prediction in large-scale ssd deployment", "2021 51st Annual IEEE/IFIP International Conference on Dependable Systems and Networks (DSN)", pp. 263–270, 2021, doi:10.1109/DSN48987.2021.00039.
- [3] J. Sevilla, L. Heim, A. Ho, T. Besiroglu, M. Hobbhahn, P. Villalobos, "Compute trends across three eras of machine learning", "2022 International Joint Conference on Neural Networks (IJCNN)", pp. 1–8, 2022, doi:10.1109/IJCNN55064.2022.9891914.

- [4] S. Maneas, K. Mahdavian, T. Emami, B. Schroeder, "A study of SSD reliability in large scale enterprise storage deployments", "18th USENIX Conference on File and Storage Technologies (FAST 20)", pp. 137–149, USENIX Association, Santa Clara, CA, 2020.
- [5] M. T. Ribeiro, S. Singh, C. Guestrin, "“why should i trust you?": Explaining the predictions of any classifier", "Proceedings of the 22nd ACM SIGKDD International Conference on Knowledge Discovery and Data Mining", KDD '16, p. 1135–1144, Association for Computing Machinery, New York, NY, USA, 2016, doi:[10.1145/2939672.2939778](https://doi.org/10.1145/2939672.2939778).
- [6] S. M. Lundberg, S.-I. Lee, "A unified approach to interpreting model predictions", I. Guyon, U. V. Luxburg, S. Bengio, H. Wallach, R. Fergus, S. Vishwanathan, R. Garnett, eds., "Advances in Neural Information Processing Systems", vol. 30, Curran Associates, Inc., 2017.
- [7] B. C. Cheong, "Transparency and accountability in ai systems: safeguarding wellbeing in the age of algorithmic decision-making", *Frontiers in Human Dynamics*, vol. Volume 6 - 2024, 2024, doi:[10.3389/fhumd.2024.1421273](https://doi.org/10.3389/fhumd.2024.1421273).
- [8] L. Lin, C. Walker, V. Agarwal, "Explainable machine-learning tools for predictive maintenance of circulating water systems in nuclear power plants", *Nuclear Engineering and Technology*, vol. 57, no. 9, p. 103588, 2025, doi:<https://doi.org/10.1016/j.net.2025.103588>.
- [9] B. Lund, T. Wang, N. R. Mannuru, B. Nie, S. Shimray, Z. Wang, "Standards, frameworks, and legislation for artificial intelligence (ai) transparency", *AI and Ethics*, pp. 1–17, 2025, doi:[10.1007/s43681-025-00661-4](https://doi.org/10.1007/s43681-025-00661-4).
- [10] A. Batool, D. Zowghi, M. Bano, "Ai governance: a systematic literature review", *AI and Ethics*, pp. 1–15, 2025, doi:[10.1007/s43681-024-00653-w](https://doi.org/10.1007/s43681-024-00653-w).
- [11] J. Jakubowski, et al., "Performance of explainable ai methods in asset failure prediction", "Computational Science – ICCS 2022", pp. 1–14, Springer, Cham, Switzerland, 2022, doi:[10.1007/978-3-031-08760-8_40](https://doi.org/10.1007/978-3-031-08760-8_40).
- [12] F. Amato, et al., "A comparative assessment of explainable ai tools in predicting hard disk drive health", "Symposium on Advanced Database Systems (SEBD)", pp. 574–584, Villasimius, Italy, 2024.
- [13] B. Goodman, S. Flaxman, "European union regulations on algorithmic decision-making and a "right to explanation"", *AI Magazine*, vol. 38, no. 3, pp. 50–57, 2017, doi:[10.1609/aimag.v38i3.2741](https://doi.org/10.1609/aimag.v38i3.2741).
- [14] European Parliament and Council, "Regulation (eu) 2024/1689 laying down harmonised rules on artificial intelligence", 2024, available: <https://eur-lex.europa.eu/eli/reg/2024/1689/oj>.
- [15] National Institute of Standards and Technology, "Ai risk management framework (ai rmf 1.0)", Tech. Rep. NIST AI 100-1, U.S. Department of Commerce, Washington, DC, USA, 2023, available: <https://nvlpubs.nist.gov/nistpubs/ai/NIST.AI.100-1.pdf>.
- [16] European Union Agency for Fundamental Rights, *Data protection and AI: The right to explanation in practice*, Publications Office of the European Union, Luxembourg, 2022, available: <https://fra.europa.eu/en/publication/2022/artificial-intelligence-right-to-explanation>.
- [17] Cybersecurity and Infrastructure Security Agency, "Secure and resilient ai framework", Tech. rep., U.S. Department of Homeland Security, Washington, DC, USA, 2024, available: <https://www.cisa.gov/resources-tools/resources/secure-and-resilient-ai-framework>.
- [18] Y. Zhang, et al., "Multi-view feature-based ssd failure prediction: what, when, and why", "USENIX Conference on File and Storage Technologies (FAST)", pp. 409–424, Santa Clara, CA, USA, 2023.
- [19] E. Pinheiro, W.-D. Weber, L. A. Barroso, "Failure trends in a large disk drive population", "USENIX Conference on File and Storage Technologies (FAST)", pp. 17–29, San Jose, CA, USA, 2007.
- [20] B. Schroeder, G. A. Gibson, "Disk failures in the real world: what does an mttf of 1,000,000 hours mean?", "USENIX Conference on File and Storage Technologies (FAST)", pp. 1–16, San Jose, CA, USA, 2007.
- [21] F. Mahdisoltani, I. Stefanovici, B. Schroeder, "Predicting disk replacement toward reliable data centers", "USENIX Annual Technical Conference (ATC)", pp. 609–622, Santa Clara, CA, USA, 2017.
- [22] J. Wen, Y. Zhang, X. Wang, Z. Chen, "A deep learning approach for hard drive failure prediction", "IEEE International Conference on Big Data", pp. 3174–3182, Seattle, WA, USA, 2018.
- [23] V. Luković, Z. Jovanović, S. Đurašević Pešović, U. Pešović, B. Đorđević, "Solid-state drive failure prediction using anomaly detection", *Electronics*, vol. 14, no. 7, 2025, doi:[10.3390/electronics14071433](https://doi.org/10.3390/electronics14071433).
- [24] J. Xiao, Z. Xiong, S. Wu, Y. Yi, H. Jin, K. Hu, "Disk failure prediction in data centers via online learning", "Proceedings of the 47th International Conference on Parallel Processing", ICPP '18, Association for Computing Machinery, New York, NY, USA, 2018, doi:[10.1145/3225058.3225106](https://doi.org/10.1145/3225058.3225106).
- [25] C. Lu, K. Ye, G. Xu, C.-Z. Xu, T. Bai, "Imbalance in the cloud: An analysis on alibaba cluster trace", "2017 IEEE International Conference on Big Data (Big Data)", pp. 2884–2892, 2017, doi:[10.1109/BigData.2017.8258257](https://doi.org/10.1109/BigData.2017.8258257).
- [26] N. V. Chawla, K. W. Bowyer, L. O. Hall, W. P. Kegelmeyer, "Smote: synthetic minority over-sampling technique", *Journal of Artificial Intelligence Research*, vol. 16, pp. 321–357, 2002, doi:[10.1613/jair.953](https://doi.org/10.1613/jair.953).

Copyright: This article is an open access article distributed under the terms and conditions of the Creative Commons Attribution (CC BY-SA) license (<https://creativecommons.org/licenses/by-sa/4.0/>).

Appendix

A. Feature Correlation Clusters and Domain-Guided Selection

This appendix describes the correlation clusters identified during exploratory analysis and the domain-informed rationale used to select representative SMART attributes.

A.1. Cluster 1: Power & Program Failures

Within this group, four correlated features were identified: n_{12} , n_{171} , n_{172} , and n_{174} . While n_{12} (Power Cycle Count) represents the number of times a host has been rebooted, n_{174} (Unexpected Power Loss Count) captures unsafe shutdown events. Since n_{174} is a subset of n_{12} and directly reflects critical failure conditions such as data corruption, mapping errors, and circuit stress, it was retained while n_{12} was eliminated.

Additionally, n_{171} (Program Fail Count) and n_{172} (Erase Fail Count) exhibit 99.9% correlation with n_{174} , indicating that failures in this dataset are strongly driven by power-loss events. Therefore, both features were removed in favor of n_{174} .

A.2. Cluster 2: Wear & Age Cluster

This cluster includes six correlated features: n_9 , n_{177} , n_{181} , n_{182} , n_{244} , and n_{245} . The feature n_9 (Power-On Hours) represents device age, while the remaining features capture various vendor-specific wear and lifespan indicators.

Specifically, n_{177} (Wear Leveling Count) shows a strong inverse correlation of -0.9798 with n_9 . Similarly, n_{244} (Total LBAs Read Expanded) and n_{245} (Remaining

Rated Write Endurance) exhibit strong inverse correlations of -0.9849 with n_9 . Additionally, n_{181} and n_{182} (Program/Erase Fail Counts) are duplicates of previously removed features and show inverse correlation of -0.985 with n_9 .

Consequently, these five features were eliminated in favor of n_9 , which provides a standardized and continuous representation of device age, enabling the model to distinguish between early-life failures and wear-out behavior.

A.3. Cluster 3: Critical Error Reporting

This cluster consists of three correlated features: n_{184} , n_{187} , and n_{197} . The feature n_{197} (Current Pending Sector Count) is the most informative, as it dynamically tracks sectors awaiting remapping due to read failures.

Both n_{184} (End-to-End Error) and n_{187} (Reported Uncorrectable Errors) exhibit strong correlations of 0.9833 and 0.9934 with n_{197} , respectively. This suggests that uncorrectable errors are typically preceded by an accumulation of pending sectors.

Therefore, n_{184} and n_{187} were removed in favor of n_{197} , which serves as an early indicator of degradation and provides a more granular signal for failure prediction.

A.4. Cluster 4: Communication Timeouts

This cluster includes two highly correlated features: n_{188} and n_{198} . The feature n_{188} (Command Timeout) tracks aborted operations due to device unresponsiveness, while n_{198} (Offline Uncorrectable Sector Count) captures uncorrectable errors detected during background scans.

With a near-perfect correlation of 0.9999 , this relationship indicates that command timeouts are largely driven by underlying media errors. Therefore, n_{188} was eliminated in favor of n_{198} , which provides a more direct measure of hardware failure.

A.5. Cluster 5: Emergency Actions & Wear-Out

This cluster contains three correlated features: n_{192} , n_{232} , and n_{233} . The feature n_{192} (Emergency Retract Count) reflects abrupt shutdown events, while n_{232} (Available Reserved Space) and n_{233} (Media Wear-Out Indicator) measure NAND endurance.

As reserved space depletion directly limits the drive's ability to recover from errors, n_{232} serves as a critical in-

dicator of failure. Both n_{192} and n_{233} exhibit extremely high correlations of 0.9998 and 0.9993 with n_{232} .

Accordingly, n_{192} and n_{233} were removed in favor of n_{232} .

A.6. Cluster 6: Workload vs. Repair Activity

This cluster includes three correlated features: n_{196} , n_{241} , and n_{242} . While n_{241} (Total LBA Written) and n_{242} (Total LBA Read) measure workload intensity, n_{196} (Reallocation Event Count) reflects actual repair activity.

Both workload features exhibit strong inverse correlations of -0.9658 with n_{196} . Since n_{196} directly captures hardware recovery behavior, it was retained while n_{241} and n_{242} were eliminated.

A.7. Cluster 7: Bad Block Management

The final cluster consists of two correlated features: n_5 and n_{183} . The feature n_5 (Reallocated Sectors Count) tracks the cumulative number of replaced sectors, while n_{183} (Runtime Bad Block) represents detected bad blocks.

With a correlation of 0.9521 , both features provide similar information. However, n_5 is a widely recognized and standardized reliability indicator in SSD failure prediction literature. Therefore, n_{183} was removed in favor of n_5 .

Biography



SAURAV KANT KUMAR is currently pursuing a Ph.D. in Artificial Intelligence at the University of the Cumberland. He has over eight years of industry experience in artificial intelligence, working in roles ranging from Data Scientist to Machine Learning Engineer. His professional experience spans multiple domains, including Banking, Telecommunications, Healthcare, Manufacturing, Supply Chain, Oil & Gas, and High Performance Computing.

His research experience focuses on predictive maintenance in high-performance computing environments and the application of machine learning and explainable AI to large-scale infrastructure data. His research interests include predictive maintenance, explainable AI, generative AI, agentic AI, and scalable machine learning for high-performance computing and large-scale systems.

An Extended Investigation of Detergent Bottle Structure Based on Fluid Mechanics

Yeonwoo Kwon¹, Eunsung Jekal²

¹Independent researcher, South Korea

²Jekal's Laboratory, Department of Physics, Ulsan, South Korea

Email(s): ywkwon@gmail.com (Y. Kwon) , everjekal@gmail.com (E. Jekal)

*Corresponding author: Eunsung Jekal, Jekal's Laboratory, department of Physics, Ulsan, South Korea, +82 10 3837 4733 & everjekal@gmail.com

ABSTRACT: This study aims to quantitatively evaluate how structural design factors of liquid detergent bottles—such as the size, position, and shape of the outlet hole, material, and the presence of an air vent—affect the discharge characteristics of viscous detergents from the perspective of fluid mechanics. Using hydrostatic pressure and Bernoulli's principle, we theoretically derive the influence of head differences and cross-sectional area on the outlet velocity. Python-based numerical simulations were conducted using a wide range of outlet radii (0.3–2.0 cm), outlet heights (2–18 cm), viscosity-dependent discharge coefficients ($C_d = 0.45\text{--}0.92$), and time-dependent variations in fluid level $h(t)$. Additional experiments comparing outlet shapes (circular, elliptical, slit-type) and the presence of an air vent were also performed. Results show that outlet radius is the dominant factor in discharge volume ($Q \propto r^2$), whereas outlet height has a moderate influence, increasing velocity proportionally to \sqrt{h} . Higher viscosity significantly reduced actual discharge (50–80% of the theoretical value). The existence of an air vent greatly improved discharge stability. This study demonstrates the value of applying fluid mechanics to everyday household product design and provides essential insights for developing automatic detergent dispensers and advanced viscous-fluid control systems.

KEYWORDS: Hydrostatic Pressure, Python coding

1. Introduction

Containers that store and discharge liquids from modern industrial products play an essential role in various fields such as food and beverage, household chemical products, cosmetics, and pharmaceuticals [1]. The functional completeness of these products is greatly influenced not only by the quality of the contents, but also by the convenience and stability during the use process. In particular, the size and shape of the outlet (hole) through which the liquid is discharged to the outside act as a key factor in determining the use experience. If the exit design is not appropriate, various problems such as excessive discharge, leakage, abnormal eruptions, and hygiene problems occur, which directly affect product reliability and consumer satisfaction [2]. Liquid container outlet design is more than just a matter of determining geometric dimensions. Hydrodynamic factors such as pressure inside the container, external atmospheric pressure, and gravitational hydrostatic pressure are combined, in addition to properties such as fluid viscosity, density, and surface tension. For instance, in highly viscous detergents

or shampoos, a small outlet can cause excessive flow resistance, while a large outlet in a dilute drink can lead to an uncontrollable state due to a sudden increase in flow rates [3]. Additionally, when liquid is discharged, the flow is intermittently cut off if the same volume of air does not flow smoothly. These problems appear frequently in everyday use situations and suggest that detailed consideration is needed at the design stage. Furthermore, since the outlet is a part that directly contacts the external environment, it has an important meaning in terms of hygiene and airtightness. Vibration, temperature changes, and air pressure changes in transportation and storage increase the risk of leakage, and contamination and residue accumulation may occur in the process of repeated use. At the same time, the outlet structure must be suitable for mass production processes and recycling systems, so manufacturing cost and structural simplicity are also considered [4]. As such, the liquid container outlet design can be said to be a comprehensive engineering problem that combines fluid mechanics, material engineering, sanitary engineering, ergonomics, and industrial design. Therefore, this study

systematically organizes the main problems that arise when designing a liquid container outlet and seeks engineering solutions for each problem. Through this, the scientific and engineering principles inherent in everyday product design are reviewed, and the necessity of rational and efficient design standards is suggested [5-6].

This study aims to quantitatively evaluate how structural design factors of liquid detergent bottles—such as the size, position, and shape of the outlet hole, material, and the presence of an air vent—affect the discharge characteristics of viscous detergents from the perspective of fluid mechanics [7]. Using hydrostatic pressure and Bernoulli's principle, we theoretically derive the influence of head differences and cross-sectional area on the outlet velocity [8]. Python-based numerical simulations were conducted using a wide range of outlet radii (0.3–2.0 cm), outlet heights (2–18 cm), viscosity-dependent discharge coefficients ($C_d=0.45-0.92$), and time-dependent variations in fluid level $h(t)$. Additional experiments comparing outlet shapes (circular, elliptical, slit-type) and the presence of an air vent were also performed. Results show that outlet radius is the dominant factor in discharge volume ($Q \propto r^2$), whereas outlet height has a moderate influence, increasing velocity proportionally to \sqrt{h} . Higher viscosity significantly reduced actual discharge (50–80% of the theoretical value). The existence of an air vent greatly improved discharge stability [9]. This study demonstrates the value of applying fluid mechanics to everyday household product design and provides essential insights for developing automatic detergent dispensers and advanced viscous-fluid control systems [10-11].

2. Theoretical Background

2.1. Hydrostatic Pressure and Head

The hydrostatic pressure at depth h is:

$$P = \rho gh$$

This implies that a lower outlet position (larger h) yields higher discharge velocity.[12]

2.2. Bernoulli's Equation and Torricelli's Law

For an orifice discharging into the atmosphere:

$$v = \sqrt{2gh}$$

Thus velocity scales with the square root of head height.

2.3. Flow Rate Equation

$$Q = Av = \pi r^2 \sqrt{2gh}$$

Hence, doubling radius yields a fourfold increase in flow rate.

2.4. Viscous Correction via Discharge Coefficient

$$Q_{\text{real}} = C_d A \sqrt{2gh}$$

C_d depends on viscosity and outlet geometry.

3. Methodology

3.1. Simulation Variables

Table 1: Range of simulation variables including outlet geometry, discharge coefficient and initial head condition

Variable	Range
Outlet radius	0.3, 0.7, 1.0, 2.0 cm
Outlet height	2–18 cm
Discharge coefficient	$C_d = 0.45-0.92$
Outlet shapes	Circular, elliptical, slit-type
Air vent	Present / absent
Initial head	15 cm

3.2. Tools

- Python
- NumPy
- Matplotlib

Simulations produced velocity, flow rate, viscosity-modified flow, and time-dependent changes.

4. Results and Extended Experiments

4.1. Effect of Outlet Height

4.1.1. Interpretation

- As head height increases, flow rate increases monotonically.
- Larger radii amplify the effect more strongly.
- Radius exhibits far stronger influence than outlet height.

4.2. Effect of Outlet Radius

4.2.1. Interpretation

- Matches theoretical $Q \propto r^2$ prediction.
- Beyond 2 cm, flow becomes excessive for household applications.

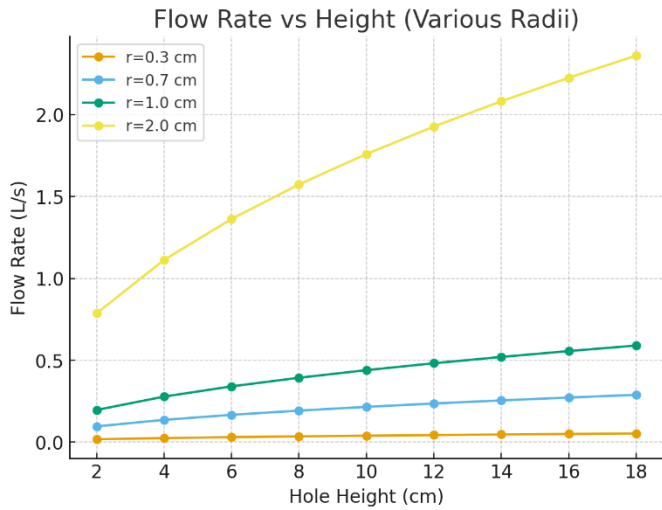


Figure 1: Flow rate vs. outlet height for different radii

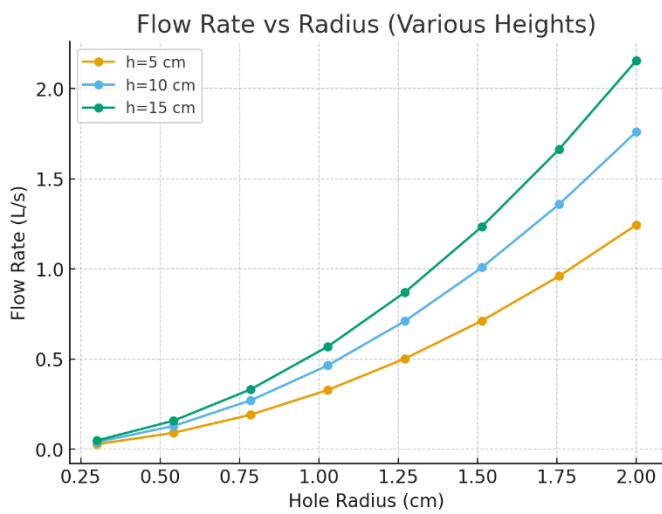


Figure 2: Flow rate vs. outlet radius for different heights

4.3. Heatmap of Height × Radius Interaction

4.3.1. Interpretation

- Highest discharge occurs in the upper-right region (large radius, deep outlet).
- Optimal design appears around $r = 1.0$ cm and $h = 10\text{--}12$ cm.

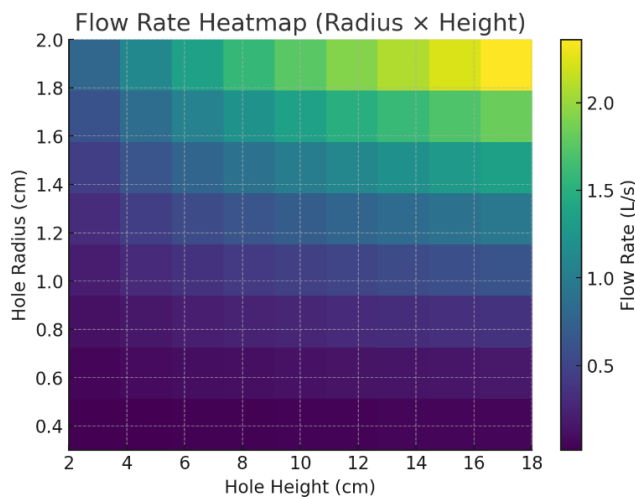


Figure 3: Flow rate heatmap across radius and height

4.4. Viscosity-Dependent Discharge

4.4.1. Interpretation

- High viscosity significantly reduces flow rate.
- Real-world discharge may be only 55–80% of theoretical predictions.
- For viscous detergents, moderate radius expansion is necessary.

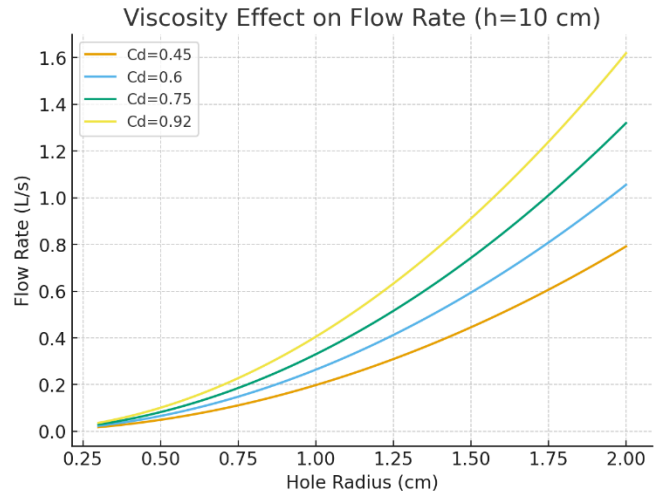


Figure 4: Flow rate variation under different discharge coefficients C_d

4.5. Time-Dependent Head Loss

4.5.1. Interpretation

- Flow rate decays nonlinearly over time as fluid level decreases.
- Explains why discharge weakens when bottle content is low.
- Automatic dispensers must incorporate compensation algorithms.

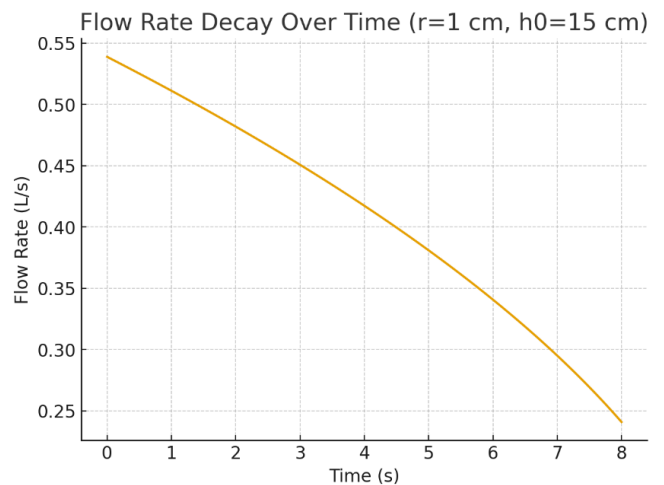


Figure 5: Flow decay as head height decreases over time

5. Additional Experimental Models

5.1. Effect of Viscosity

Table 2: Variation of real flow rate with discharge coefficient representing viscosity effects

Cd	Real Flow (L/s)
0.92	0.047
0.75	0.038
0.60	0.030
0.45	0.023

Higher viscosity → lower flow.

5.2. Effect of Outlet Shape

Table 3: Change in flow rate due to outlet geometry (circular, elliptical, slit-type)

Shape	Change in Flow
Circular	Baseline
Elliptical	+10–15%
Slit-type	–5–10%

5.3. Effect of Air Vent

Table 4: Comparison of flow stability and transient response with and without air venting

Condition	Stability	Initial Flow
With vent	Very stable	Gradual increase
Without vent	Pressure fluctuation	Spike then drop

Air venting is crucial for consistent discharge.

6. Discussion

Integrated findings indicate: Outlet radius is the dominant design parameter (exponential effect). Outlet height moderately affects discharge, increasing with \sqrt{h} . Viscosity drastically suppresses real flow, necessitating larger openings. Air vents stabilize pressure, improving usability. Time-dependent head loss requires compensation mechanisms for automated systems.

Optimal design for household bottles:

- Radius: 1.0–1.2 cm
- Outlet height: mid-level (10–12 cm)
- Air vent: mandatory
- Shape: circular preferred

7. Conclusion

This study systematically applied fluid mechanics to analyze how structural elements of detergent bottles influence discharge performance. Numerical simulations and extended experiments demonstrate that outlet radius and viscosity play the largest roles, with outlet height and venting providing secondary but meaningful effects. These findings provide fundamental design principles for efficient, stable, and user-friendly detergent dispensing systems and may inform the development of smart dispensing devices and viscous fluid control technologies.

8. Appendix: Summary Tables

Table 5: Summary of Structural Factors and Their Effects

Factor	Effect on Flow
Radius r	Major increase ($Q \propto r^2$)
Height h	\sqrt{h} increase in velocity
Viscosity	Reduces real flow
Air vent	Stabilizes flow
Hole shape	Modifies flow distribution

9. Appendix: Python codes

Detergent Bottle Flow Simulation

Language: Python 3.x

Packages: numpy, matplotlib

```
import numpy as np
```

```
import matplotlib.pyplot as plt
```

```
# 1. Physical constants and basic functions
```

```
g = 9.8 # gravitational acceleration (m/s^2)
```

```
rho = 1050 # detergent density (kg/m^3) - not directly used, but kept for completeness
```

```
def outlet_velocity(h):
```

```
    """
```

```
    Compute outlet velocity from Torricelli's law.
```

```
    h : head (m)
```

```
    v : velocity (m/s)
```

```
    """
```

```
    return np.sqrt(2 * g * h)
```

```
def theoretical_flow_rate(r, h):
```

```
    """
```

```
    Ideal flow rate (without viscosity),  $Q = A * v$ .
```

```
    r : outlet radius (m)
```

```
    h : head (m)
```

```
    return Q in m^3/s
```

```
    """
```

```
    A = np.pi * r**2
```

```
    v = outlet_velocity(h)
```

```

return A * v
def real_flow_rate(r, h, Cd):
    """
    Realistic flow rate with discharge coefficient.
    Cd : discharge coefficient (0 < Cd <= 1)
    """
    return Cd * theoretical_flow_rate(r, h)
# 2. Figure 1 – Flow vs Height (for several radii)
def figure1_flow_vs_height():
    heights = np.linspace(0.02, 0.18, 9) # 2 cm to 18 cm
    radii = [0.003, 0.007, 0.01, 0.02] # 0.3, 0.7, 1.0, 2.0 cm
    plt.figure(figsize=(7, 5))
    for r in radii:
        Q = theoretical_flow_rate(r, heights) # m^3/s
        Q_L = Q * 1000 # L/s
        plt.plot(heights * 100, Q_L, marker='o', label=f'r = {r*100:.1f} cm")
    plt.title("Flow Rate vs Outlet Height (Various Radii)")
    plt.xlabel("Outlet Height h (cm)")
    plt.ylabel("Flow Rate Q (L/s)")
    plt.grid(True)
    plt.legend()
    plt.tight_layout()
    plt.show()
# 3. Figure 2 – Flow vs Radius (for several heights)
def figure2_flow_vs_radius():
    radii = np.linspace(0.003, 0.02, 8) # 0.3–2.0 cm
    heights = [0.05, 0.10, 0.15] # 5, 10, 15 cm

    plt.figure(figsize=(7, 5))
    for h in heights:
        Q = theoretical_flow_rate(radii, h)
        Q_L = Q * 1000
        plt.plot(radii * 100, Q_L, marker='o', label=f'h = {h*100:.0f} cm")
    plt.title("Flow Rate vs Outlet Radius (Various Heights)")
    plt.xlabel("Outlet Radius r (cm)")
    plt.ylabel("Flow Rate Q (L/s)")
    plt.grid(True)
    plt.legend()
    plt.tight_layout()
    plt.show()
# 4. Figure 3 – Heatmap (Radius × Height)
def figure3_heatmap_radius_height():
    heights = np.linspace(0.02, 0.18, 9) # 2–18 cm
    radii = np.linspace(0.003, 0.02, 8) # 0.3–2.0 cm
    H, R = np.meshgrid(heights, radii)
    Q = theoretical_flow_rate(R, H) * 1000 # L/s
    plt.figure(figsize=(7, 5))
    im = plt.imshow(
        Q,
        extent=[heights.min()*100, heights.max()*100,
                radii.min()*100, radii.max()*100],
        origin='lower',
        aspect='auto'
    )
    plt.colorbar(im, label="Flow Rate Q (L/s)")
    plt.title("Flow Rate Heatmap (Radius × Height)")
    plt.xlabel("Outlet Height h (cm)")
    plt.ylabel("Outlet Radius r (cm)")
    plt.grid(False)
    plt.tight_layout()
    plt.show()
# 5. Figure 4 – Viscosity Effect (different Cd)
def figure4_viscosity_effect():
    radii = np.linspace(0.003, 0.02, 100) # 0.3–2.0 cm
    h = 0.10 # 10 cm
    Cd_values = [0.45, 0.60, 0.75, 0.92] # high viscosity → low Cd
    plt.figure(figsize=(7, 5))
    for Cd in Cd_values:
        Q = real_flow_rate(radii, h, Cd) * 1000
        plt.plot(radii * 100, Q, label=f'Cd = {Cd}')
    plt.title("Viscosity Effect on Flow Rate (h = 10 cm)")
    plt.xlabel("Outlet Radius r (cm)")
    plt.ylabel("Flow Rate Q (L/s)")
    plt.grid(True)
    plt.legend()
    plt.tight_layout()
    plt.show()
# 6. Figure 5 – Time Decay of Flow (decreasing head)
def figure5_time_decay():
    r = 0.01 # 1 cm
    h0 = 0.15 # initial head 15 cm
    t_end = 8.0 # simulate 8 seconds
    n_pts = 100
    # Simple linear decrease model for head: h(t) = h0 - k * t
    # (In reality, this is slightly nonlinear, but this is
    enough
    # to visualize the general trend.)
    times = np.linspace(0, t_end, n_pts)
    k = h0 / (t_end + 2.0) # chosen so that h stays
    positive
    h_t = np.maximum(h0 - k * times, 0.0)
    Q_t = theoretical_flow_rate(r, h_t) * 1000 # L/s
    plt.figure(figsize=(7, 5))
    plt.plot(times, Q_t)
    plt.title("Flow Rate Decay Over Time (r = 1 cm, h0 = 15 cm)")
    plt.xlabel("Time t (s)")
    plt.ylabel("Flow Rate Q(t) (L/s)")

```

```
plt.grid(True)
plt.tight_layout()
plt.show()
7. Convenience function to run all figures at once
def run_all_simulations():
    figure1_flow_vs_height()
    figure2_flow_vs_radius()
    figure3_heatmap_radius_height()
    figure4_viscosity_effect()
    figure5_time_decay()
if __name__ == "__main__":
    # Call this to reproduce all main figures in the paper
    run_all_simulations()
```

10. Future Work

While this study provides a comprehensive investigation into the influence of detergent bottle structural parameters on discharge performance using classical fluid mechanics and numerical simulations, several areas remain open for further exploration.

First, the present model employs simplified assumptions, including incompressible steady flow and a constant discharge coefficient (Cd). Future research should incorporate advanced computational fluid dynamics (CFD) simulations to account for complex internal flow structures, turbulent transitions near the outlet, free-surface deformation, and multiphase interactions between air and liquid during discharge. Such approaches would yield more precise predictions under realistic operating conditions [12].

Second, the rheological behavior of detergents was approximated using constant-viscosity coefficients. However, most detergents exhibit non-Newtonian properties such as shear-thinning or viscoelastic behavior. Future studies should directly characterize detergent rheology and integrate non-Newtonian constitutive models to better describe actual discharge dynamics [13].

Third, experimental validation can be significantly expanded. High-speed imaging, flow visualization techniques, and volumetric flow sensors could be applied to capture transient jet formation, pulsation effects caused by air entrapment, and precise time-dependent flow rates. These detailed measurements would enable refinement of discharge coefficients and direct calibration of numerical models.

Fourth, the interaction between ergonomic design and fluid performance remains largely unexplored. Future work may incorporate user handling behavior—tilting angles, gripping motions, and squeeze forces—to evaluate

how real-world usage alters discharge patterns and optimal structural parameters [14].

Lastly, future research should extend beyond manual detergent bottles toward fully automated dispensing systems. Incorporating electronic flow sensors, adaptive control algorithms, and real-time compensation for head loss or viscosity variations would enable the development of smart dispensing devices that automatically regulate dosage with high precision and repeatability [15].

Collectively, these investigations would build upon the foundation established by the present study and contribute to the development of next-generation liquid dispensing technologies optimized through both fluid mechanical principles and human-centered design.

References

- [1] T. A. Witten, "Structured fluids," *Physics Today*, vol. 43, no. 7, pp. 21-28, 1990. doi: 10.1063/1.881249.
- [2] M. Contino, *Long Term Fracture Behaviour of HDPE for Household Detergent Containers: A Study on Environmental Stress Cracking*, Ph.D. dissertation, Politecnico di Milano, Milan, Italy, 2018.
- [3] R. S. Rounds, "The manufacture of liquid detergents," in *Liquid Detergents*, 2nd ed., K.-Y. Lai, Ed. Boca Raton, FL, USA: CRC Press, 2005, pp. 657-692. doi: 10.1201/9781420027907-18.
- [4] H. C. Mayer, "Bottle emptying: A fluid mechanics and measurements exercise for engineering undergraduate students," *Fluids*, vol. 4, no. 4, Art. no. 183, 2019. doi: 10.3390/fluids4040183.
- [5] R. S. Rounds, "Rheology of liquid detergents," in *Liquid Detergents*, 2nd ed., K.-Y. Lai, Ed. Boca Raton, FL, USA: CRC Press, 2005, pp. 93-132. doi: 10.1201/9781420027907-8.
- [6] J. R. Landel and D. I. Wilson, "The fluid mechanics of cleaning and decontamination of surfaces," *Annual Review of Fluid Mechanics*, vol. 53, no. 1, pp. 147-171, 2021. doi: 10.1146/annurev-fluid-022820-113739.
- [7] H. R. Shahi, S. Dinarvand, M. Vahabi, A. M. Lavasani, and M. Nimafar, "Nanoparticle-enhanced cleaning assessment through hydro-thermo modeling in laundering of woven fabrics," *Case Studies in Thermal Engineering*, vol. [X], Art. no. 106914, 2025. doi: 10.1016/j.csite.2025.106914.
- [8] A. Winkler, N. Santo, M. A. Ortenzi, E. Bolzoni, R. Bacchetta, and P. Tremolada, "Does mechanical stress cause microplastic release from plastic water bottles?" *Water Research*, vol. 166, Art. no. 115082, 2019. doi: 10.1016/j.watres.2019.115082.
- [9] N. E. Munyaneza, R. Ji, A. DiMarco, J. Miscall, L. Stanley, N. Rorrer, R. Qiao, and G. Liu, "Chain-length-controllable upcycling of polyolefins to sulfate detergents," *Nature Sustainability*, vol. 7, no. 12, pp. 1681-1690, 2024. doi: 10.1038/s41893-024-01464-x.
- [10] N. E. Munyaneza, R. Ji, A. DiMarco, J. Miscall, L. Stanley, N. Rorrer, R. Qiao, and G. Liu, "Chain-length-controllable upcycling of polyolefins to sulfate detergents," *Nature Sustainability*, vol. 7, no. 12, pp. 1681-1690, 2024. doi: 10.1038/s41893-024-01464-x.
- [11] Q. Dong et al., "Depolymerization of plastics by means of electrified spatiotemporal heating," *Nature*, vol. 616, pp. 488-494, 2023. doi: 10.1038/s41586-023-05845-8.
- [12] T. Thiounn and R. C. Smith, "Advances and approaches for chemical recycling of plastic waste," *Journal of Polymer Science*, vol. 58, no. 10, pp. 1347-1364, 2020. doi: 10.1002/pol.20190261.

- [13] H. Lv, F. Huang, and F. Zhang, "Upcycling waste plastics with a C-C backbone by heterogeneous catalysis," *Langmuir*, vol. 40, no. 10, pp. 5077-5089, 2024. doi: 10.1021/acs.langmuir.3c03866.
- [14] S. Bezergianni, A. Dimitriadis, G.-C. Faussonne, and D. Karonis, "Alternative diesel from waste plastics," *Energies*, vol. 10, no. 11, Art. no. 1750, 2017. doi: 10.3390/en10111750.
- [15] Z. Dobó *et al.*, "Characterization of gasoline-like transportation fuels obtained by distillation of pyrolysis oils from plastic waste mixtures," *Energy & Fuels*, vol. 35, no. 3, pp. 2347-2356, 2021. doi: 10.1021/acs.energyfuels.0c04022.

Copyright: This article is an open access article distributed under the terms and conditions of the Creative Commons Attribution (CC BY-SA) license (<https://creativecommons.org/licenses/by-sa/4.0/>).